Thermal stress analysis of a Water-Molten Salt Heat Exchanger

Computational Fluid Dynamics with Fluid-Structure Interaction

Jakub Naider

MSc in Sustainable Energy Engineering, Process Engineering and Combustion Technology, Spring 2023

Master Thesis

STUDENT REPORT

AALBORG UNIVERSITY

LaTeX is used for formatting this report and all images which are not cited are made by the group.

AALBORG UNIVERSITY
STUDENT REPORT

Department of Energy
Aalborg university Esbjerg, Department of Energy Niel Bohrs Vej 8
DK-6700 Esbjerg
Denmark

Title:
Thermal stress analysis of a Water-Molten Salt Heat Exchanger

Theme:
Computional Fluid Dynamics, Fluid-Structure interactions

Project Period:
Spring Semester 2023

Project Group:
PECT4

Participant(s):
Jakub Naider

Supervisor(s):
Matthias Mandø

Page Numbers: 59

Date of Completion:
May 31, 2023

Abstract:

A CFD analysis has been performed for the simulation of a molten sodium hydroxide heat exchanger. Two different designs were investigated: Double pipe and U-tube heat exchangers for 3 different pressures (1,2 and 5 [bar]) of the working fluid, which was water. Then the FEM analysis of Thermal stress was performed. The simulations ran with the assumption that stress induced by constrained expansion is covered by the heat exchanger design apart from one for the atmospheric pressure for the U-tube heat exchanger. In this simulation, it was assumed that the baffle is pressed on the heat exchanger tubes and any expansion of the tubes is constrained by the baffle. Additionally, the Factor of Safety for each simulation was computed in order to find out, if the stress exceeds the tensile yield strength and thus the elastic range. The comparison between each of the scenarios revealed that considering the same properties and boundary conditions Double pipe HX produces higher amounts of thermal stress, but still keeps the levels of Factor of Safety at an acceptable level. Moreover, it has been found that it is necessary to apply safety measures to the expansion of the pipes as the Factor of Safety for a case with constrained expansion was less than 1 and thus elastic range was exceeded and the pipes are irreversibly damaged.

Summary

This thesis addresses the importance of energy storage technologies for achieving a flexible power grid that can effectively incorporate renewable energy sources. Specifically, it focuses on the potential of Molten Salt Energy Storage Systems (MOSESS) as a viable solution due to their unique thermo-physical characteristics. The primary challenge in designing MOSESS lies in managing thermal stresses resulting from temperature differentials between hot and cold fluids. To overcome this challenge, various design strategies are explored, including the use of materials with high-temperature resistance, optimization of heat exchanger geometry, and control of fluid flow rates and temperatures to minimize thermal shock. Moreover, two important heat exchanger design are investigated: Double pipe Heat exchanger and U-tube heat exchanger. The molten Sodium Hydroxide (NaOH) is investigated as the heat transfer fluid and Water as a working fluid.

Computational fluid dynamics (CFD) and fluid-structure interaction (FSI) analysis are employed to evaluate the magnitude of thermal stress and inform design modifications. The simulations reveal that different water pressure scenarios significantly influence the thermal stress and the Factor of Safety (FOS). Higher water pressure results in lower stress magnitudes and higher FOS. Furthermore, constraints on the expansion between the baffle and pipes necessitate the use of elastic parts or materials with higher tensile yield strength to avoid exceeding the elastic range.

The findings underscore the significance of proper design and operation for ensuring the safe and efficient performance of molten sodium hydroxide heat exchangers. By utilizing CFD and FSI analysis, engineers can optimize the design, ensuring that thermal stresses remain within the elastic range and selected materials are suitable for the operating conditions. Moreover, the integration of MOSESS into the power grid can be enhanced by implementing these design strategies and computational analysis techniques.

This research contributes to the knowledge base on thermal stress management in molten sodium hydroxide heat exchangers, providing insights into the advancement of energy storage technologies. However, further research and experimentation are required to validate and refine the presented findings. Nevertheless, the outcomes of this study demonstrate the potential of innovative design approaches and computational analysis tools to improve the performance, safety, and efficiency of molten sodium hydroxide heat exchangers, thus supporting the transition towards a sustainable energy future.

Preface

This study is conducted from 01/02-2023 to 20/5-2023 by a student from Process Engineering and Combustion Technology at Aalborg University, Esbjerg. The common interest is based on determining the magnitude of thermal stress at the Molten Sodium Hydroxide-Water heat exchangers and evaluating the process safety, using the knowledge and tools obtained during the Master's programme.

A special acknowledgement is given to the supervisor, Matthias Mandø for his guidance and encouragement throughout this project.

Aalborg University, May 31, 2023

Jakub Naider
<jnaide21@student.aau.dk>

Contents

Chapter 1

Introduction

Sustainable energy storage is a critical requirement for transitioning to a clean and low-carbon energy system. Among the various energy storage technologies available, thermal energy storage (TES) is an attractive option due to its high energy density, long cycle life, and low maintenance requirements. TES systems can store thermal energy generated from renewable sources, such as solar and wind, and release it as needed, thus enabling a more reliable and stable energy supply.

One of the key components of TES systems is the heat exchanger, which transfers heat between the storage medium and the working fluid. Molten Sodium hydroxide- water heat exchangers are commonly used in TES systems due to the high heat capacity and low cost of molten Sodium Hydroxide. However, the use of molten Sodium Hydroxide can also result in high thermal stresses due to the large temperature gradients and thermal expansion coefficients, which can lead to deformation and failure of the heat exchanger.

To ensure the safe and reliable operation of TES systems, it is important to understand the thermal stresses and deformations that occur in the heat exchanger during operation. In this thesis, we present a thermal stress analysis of a molten NaOH-water heat exchanger using fluid-structure interaction (FSI) simulations. The FSI simulations combine computational fluid dynamics (CFD) and Finite element method (FEM) simulations to capture the complex interactions between the fluid and the solid components of the heat exchanger.

The objectives of this thesis are to set appropriately a numerical model of the molten salt-water heat exchanger using CFD and FEM simulations. Investigate the effects of different operating conditions on the thermal stresses and deformations in the heat exchanger. Evaluate the performance of the heat exchanger under various scenarios, such as changes in the temperature of the working fluid or thickness of the tubes. The results of this study will contribute to the design and optimization of TES systems and improve our understanding of the thermal behaviour of molten NaOH- water heat exchangers.

Chapter 2

State of the art of the thermal energy storage

2.1 Energy storage technologies

Renewable energy power plants, such as wind or solar farms, are expected to replace conventional fossil fuel power plants. However, total independence in the energy sector requires more research and development. In particular, appropriate energy storage technologies need to be developed and implemented in the energy grid to deal with fluctuations in renewable energy production. Cost-effective methods for large-scale energy storage would result in a more flexible power grid. There are numerous energy storage possibilities (as can be seen on 2.1).

Mechanical	Chemical	Electrical	Thermal
Hydropumping	Batteries	Capacitor	Molten Salt
Compressed Air	Hydrogen	Superconducting Magnet	Phase-Change Material
Flywheel	Flow Batteries		Solid Media

Table 2.1: Different types of energy storage [1]

There are numerous energy storage possibilities, including mechanical, chemical, electrical, and thermal methods. Mechanical, electrical, and chemical energy are considered high-quality energy because they can be converted from one form to another directly. The goal is to achieve minimal cost while maintaining maximal energy density and charging rates at minimal energy losses and leakage [1]. Chemical and electrical methods perform well only in small-scale applications otherwise, they are not cost-effective. Mechanical storage, such as hydropumping or compressed air, has low energy density and depends on geographic location. The last type of energy is thermal, which is considered low-quality energy in the sense that during the conversion process to electrical energy, there is a fundamental thermodynamic cost.

For example, the thermoelectric generator (Seebeck generator) has a typical efficiency of around 10% [2] (with a possible conversion efficiency of around 40% at a temperature above 1900K) and the steam turbine, which converts chemicals into thermal and then electrical, has a maximum achieved efficiency of 64% (claimed by GE in 2017 [3]). While perfect energy conversion efficiency can not be achieved in real-life applications, the decisive parameter is the economical feasibility and overall profitability of the system. Figure 5.4 indicates the general application areas of current EES systems and also provides a guiding range for potential future applications.

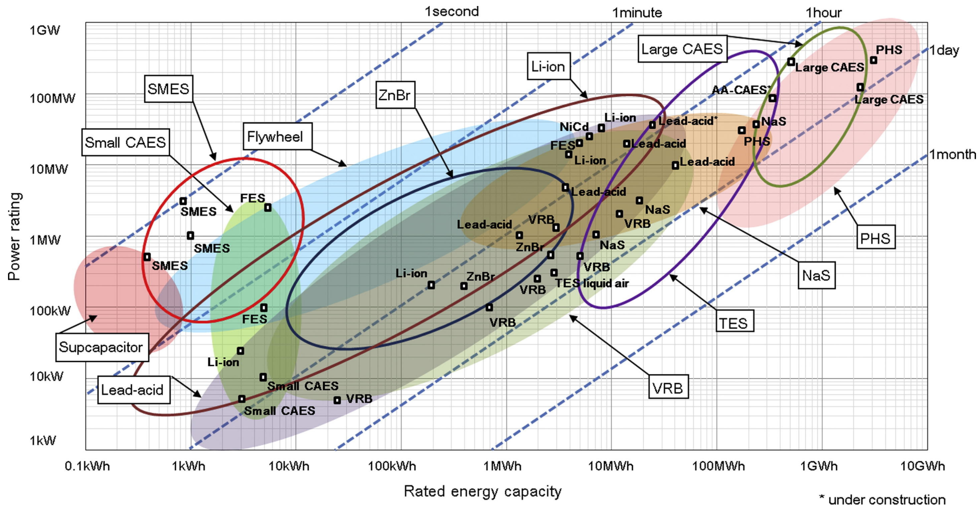

Figure 2.1: Comparison of power rating and rated energy capacity with discharge time duration at power rating. [4]

2.2 Thermal energy storage systems

Thermal storage systems store energy in the form of heat, this could be either latent or sensible heat. The energy stored by a sensible heat is considering only a single phase of the material, where the stored energy is linearly dependent on the temperature difference of the medium. The medium can be either liquid (water, oil, molten salt) or solid (rock, metal). Latent heat is the heat or energy that is absorbed or released during a phase change of a substance, either from a gas to a liquid or liquid to a solid and vice versa. It is related to enthalpy and is specified by the property-specific latent heat of the substance L. The total heat stored by the medium can be calculated as follows:

$$Q_{total} = Q_{sensible} + Q_{latent} = m \cdot C \cdot \Delta T + m \cdot L \tag{2.1}$$

where Q_{total} is the total heat stored by the medium, $Q_{sensible}$ is sensible heat, m is mass, C is the specific heat, ΔT is the temperature difference, Q_{latent} is latent heat and L is the specific latent heat for a particular substance.
Including latent heat in the energy storage system is appealing due to the higher energy storage density. Thermal energy systems can be combined with various process heat applications, such as desalination, excess electricity to meet demand at peak times, and heat supply for high-temperature processes such as H_2 production.

According to [5], sensible storage materials are more prone to leakage and exposure to corrosion. Otherwise, more safety mechanism has to be involved in the process. The usage of solid sensible storage materials like rocks or pebbles also carries another disadvantage in the form of non-uniformity of the thermal characteristics across a wide variety of rocks. Multiple parameters affect the thermal properties such as geography, mineral composition and climatic condition.

Moreover, the study showed that latent heat storage systems are more suitable for high-temperature systems. Additionally, the energy storage capacity is also higher. Phase change materials have been employed in many practical applications, such as buildings, medical applications, storage, and solar distillation. The PCMs are considered to be the most reliable, economic, and environmentally friendly method of energy storage for the future. However, the thermal conductivity of PCMs needs to be improved, which carbon-based additives have been promising in achieving. There are challenges associated with the manufacture and use of PCMs, including material compatibility, cost efficiency, thermal performance, health and safety, and safe disposal practices.

2.2.1 Molten Salt energy storage system

The Molten Salt Energy Storage System (MOSESS) has shown great potential among other energy storage systems due to its unique thermo-physical characteristics, such as a high boiling point, low viscosity, high volumetric heat capacity, and the experience already gained in renewable energy solar power plants.

The key parameters for molten salts are the highest possible temperature range between melting and freezing point, if the freezing point is too high additional heating may be required to prevent freezing, and maximizing the heat capacity of the medium will lead to a smaller storage tank volume. The common salts used for storage such as sodium nitrate ($NaNO_3$) and potassium nitrate (KNO_3) have melting points between 300-500°C and specific heat capacity from 1.2 - 1.8 [$\frac{kJ}{kgK}$] [6].

Sodium hydroxide NaOH has a melting point at 320°C and can be used up to 800°C, but is highly corrosive [7]. A mixture of salts commonly used at solar plants consists of potassium nitrate (53% by weight), sodium nitrite (40% by weight) and sodium nitrate (7% by weight) with a liquid temperature range of 149 - 538°C [8]. Comparison of different fluids can be seen on Tab.2.2.

Material	Melting point [K]	Specific heat capacity $[\frac{kJ}{kgK}]$	Thermal conductivity $[\frac{W}{mK}]$	Viscosity $[Pa \cdot s]$
Water (at 20°C)	273	4.18	0.60	0.0010
NaOH (at 400°C) [9]	591	2.26	1.08	0.0207
$LiF - BeF_2$ (700°C) [10]	733	2.41	1.00	0.0056
$NaNO_3 - KNO_3$ (at 400°C) [11]	495	2.66	0.55	0.0017

Table 2.2: Thermal properties of heat transfer fluids

The salts are stored in a heated insulating container during off-peak hours. Otherwise, the salt is pumped into the heat exchanger for steam generation and to the turbine connected to the generator for producing electricity. This can be done by either Rankine or Brayton cycles. Alternatively, the stored heat can be used for high-temperature processes such as H_2 generation or coal-to-liquid conversion, which avoids the energy losses caused by converting heat to electricity. The cooled salt is then pumped back into the storage tank to be heated and reused.

There are two different designs for the molten salt energy storage system. Two-tank direct and thermocline. The two-tank direct system is using molten salt both as heat transfer liquid and heat storage fluid and consists of two tanks one for cold and one for hot salt. The thermocline system uses a single tank such that hot and cold salt is separated by the vertical temperature gradient (due to buoyancy forces) to prevent mixing and the process consists of two cycles: charging and discharging. To charge, salt flows out of the cold side and is heated by the heat exchanger and flows into the tank's hot side. To discharge, salt flows out of the hot side, transfers heat and flows into the tank's cold side. Although, in energy storage systems the heat would be provided by electrical heaters instead of heat exchangers. The thermocline system reduces costs through a single tank and cheap filler material in the tank to act as thermal storage, the estimated cost relative to the two-tank direct system is about 35% [8, 12].

Two different designs of thermocline molten salt storage can be seen in Fig.2.2. The single-medium thermocline (SMT) uses only fluid like molten salt. The second one is dual-medium thermocline (DMT), which has economical and technical advantages over SMT tanks. The thermocline performance is most affected by the diameter of the filler materials and their properties, the velocity of the heat transfer fluid and its properties, the height-to-diameter ratio and the porosity.

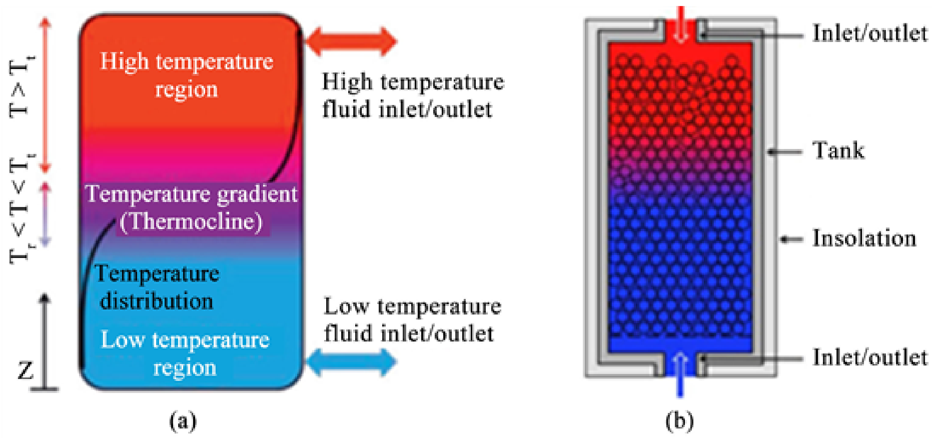

Figure 2.2: Types of thermocline storage tank a) SMT b) DMT [13]

2.3 Molten salt heat exchanger

Molten salt heat exchangers are most common in two different applications: at Nuclear facilities, where they are used to transfer heat from the primary coolant loop to the process loops. The molten salts are popular at Nuclear facilities due to exceptional thermal stability (against decomposition, boiling etc.) at temperatures up to 1000°C. The other application is Concentrated Solar Power (CSP) farms, where the heat from the sun is used to keep the salt temperature above freezing point. The CSP stands among other renewable energy sources like wind turbine farms or photo-voltaic as a possibility to incorporate a thermal energy storage system that produces electricity from the solar resource availability.

One of the most important issues molten salt heat exchangers are dealing with is the high corrosivity of the heat transfer medium. This requires using resistant materials such as Hastelloy N and Hastelloy 242 [14]. Alternatively, Inconel 625 alloy showed high resistance to corrosion even under high temperatures around 600°C [15]and proven superior to stainless steals such as 316 310 [16].

On the other hand, using molten salt as a heat transfer fluid has numerous advantages. Namely, by a quarter higher heat capacity than pressurized water, the size of a heat-transport loop is much smaller than for other coolants. The pressure inside the pipes can be much lower, which lowers the requirements for heat exchanger construction.

One of the most popular designs of heat exchangers is Shell and Tube heat exchanger, thanks to their robust geometry construction, easy maintenance and possible upgrades, as shown in Fig. 2.3.

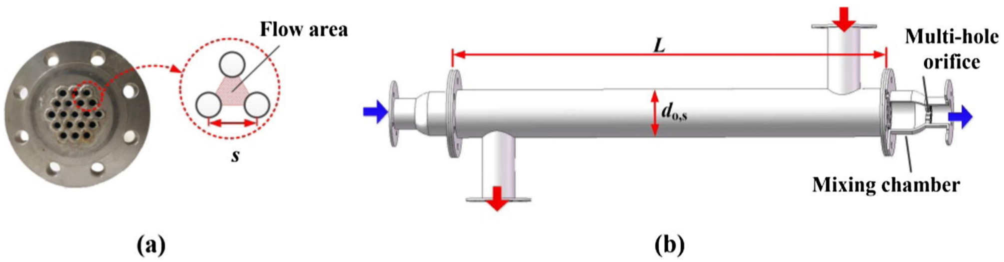

Figure 2.3: Tube and shell heat exchanger [17]

Another popular design is the U-tube Heat exchanger (viz. Fig.2.4), which is overall well suited for stable operation loads and minimum temperature changes, typical for continuous operating processes. The U-tube heat exchanger performs better in cases with different temperature profiles, which leads to different thermal expansion and is a more cost-effective alternative to floating head heat exchangers both at capital cost and maintenance.

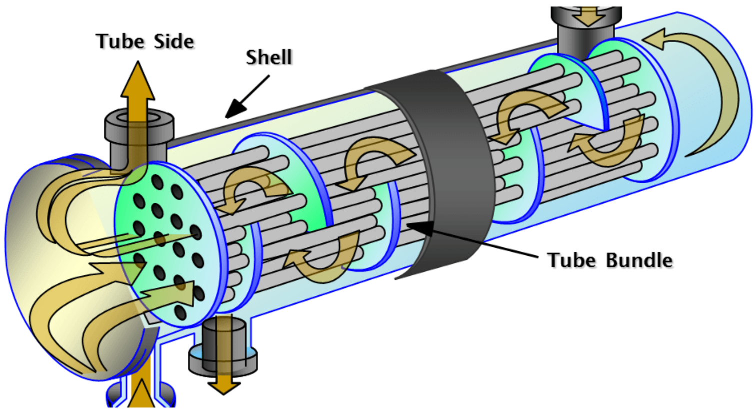

Figure 2.4: U-tube heat exchanger [18]

2.4 Thermal stress in high-temperature heat exchangers

Thermal stresses are stresses induced in a material due to temperature changes. In high-temperature heat exchangers, such stresses can arise due to the temperature gradients that occur in the heat exchanger as a result of the heat transfer process.

Thermally-induced damage is mainly caused by thermal stratification, thermal striping and thermal cycling phenomena. It typically occurs in pipe systems where the fluid flows at a low velocity with a large temperature variance. Thermal stratification occurs when two types of steam with different temperatures come into contact. Their temperature difference causes the colder and heavier water to settle at the bottom of the pipe while allowing the warmer and lighter water to float over the colder water.

When this thermal stratification phenomenon occurs, the pipe is submitted to loads due to the temperature difference between its cross-section's upper and lower regions. The upper region of the pipe tends to expand; meanwhile, its lower region opposes this expansion (viz. Fig.2.5.

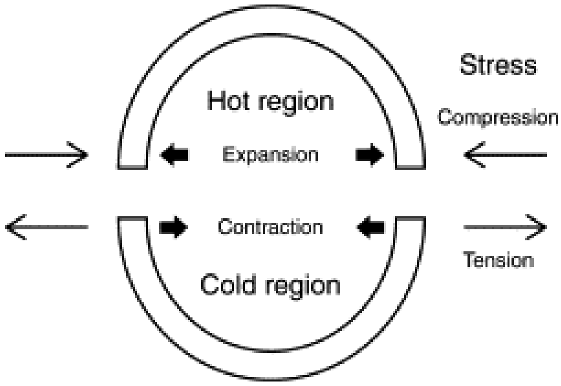

Figure 2.5: Stresses of the cross-section of the pipe under thermal stratification [19]

Another observation during thermal stratification is the local temperature variation in the fluid interface known as thermal striping. Thermal striping is a random temperature fluctuation produced by the incomplete mixing of fluid streams at differing temperatures. Structures exposed to such temperature fluctuations may suffer thermal fatigue damage. The thermal striping phenomenon is characterized by an oscillation frequency and amplitude as can be seen in Fig. 2.6.

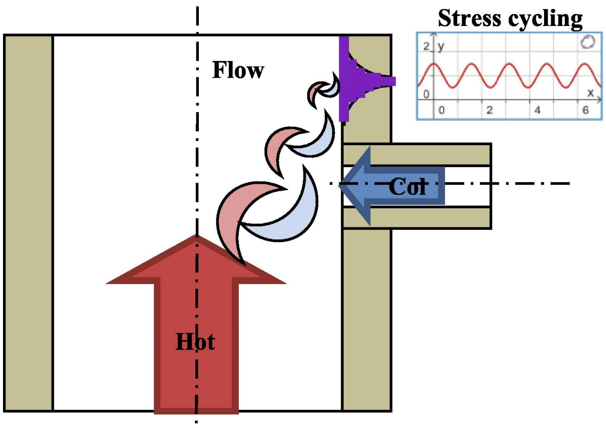

Figure 2.6: Thermal striping phenomenon with Stress cycling oscillation [20]

The third cause of damage is known as thermal cycling. This can occur when the piping system undergoes a transient operational event, or when turbulence in the main pipe interacts with the thermally stratified layer in a branch pipe. It causes the boundary between the two regions to fluctuate.

Various design strategies can be employed to mitigate thermal stresses in high-temperature heat exchangers. These may include selecting materials with similar coefficients of thermal expansion, designing the heat exchanger to accommodate differential expansion, and incorporating features such as thermal insulation and thermal expansion joints. Also, proper operation and maintenance of the heat exchanger can help minimise thermal stresses.

As mentioned in a recent publication by Luo et al. [21] on the analysis of thermal stress in 2022, the temperature disparity between the ongoing and shutdown phases of the molten salt energy storage process can generate thermal stress. This stress can cause fatigue or creep damage, leading to leakage of the heat transfer medium, if it surpasses the critical stress limit of the material. Further research reveals that at temperatures of approximately 600°C, the thermal stress can climb to a level as high as 245MPa, underscoring the importance of utilizing durable materials in high-temperature processes.

Chapter 3

Problem Statement

The text presented in the previous chapter discusses the importance of energy storage technologies in achieving a more flexible power grid. Renewable energy sources such as wind and solar farms are becoming an influential part of the energy grid. However, the natural fluctuation in electricity generation does not generally coincide with the electricity demand. To deal with this issue, economically viable large-scale energy storage methods need to be integrated into the power grid.

Molten Salt Energy Storage System (MOSESS) is a type of thermal energy storage system that has shown great potential due to its unique thermo-physical characteristics. The critical parameters for molten salts are the highest possible temperature range between melting and freezing points and maximizing the heat capacity of the fluid. Another important parameter to investigate is the thermal conductivity of the solid materials.

One of the major challenges in designing a molten salt heat exchanger is managing the thermal stresses that can occur due to the large temperature differences between the hot and cold fluids. These stresses can cause deformation or failure of the heat exchanger, which can be costly and dangerous. In the simulated cases, the temperature gradients are caused by the temperature difference between the storage fluid (NaOH) and the working fluid (water), which is assumed to be at boiling point at the outer walls of pipes. Thus the magnitude of temperature at the boiling point will vary with pressure together with the thermal stress.

Various design strategies can be employed to mitigate thermal stresses in molten salt heat exchangers, such as using materials with high-temperature resistance, optimizing the geometry of the heat exchanger to reduce thermal gradients, and controlling the flow rate and temperature of the fluids to minimize thermal shock.

Overall, proper design and careful operation are essential for ensuring the safe and efficient operation of molten salt heat exchangers, and thermal stress management is a critical aspect of this. CFD and FSI analysis can be valuable tools for ensuring the design quality of molten salt heat exchangers. These techniques can help determine the magnitude of thermal stress, providing insights into the suitability of materials and the need for modifications to the heat exchanger's geometry. By using CFD and FSI analysis, engineers can make informed decisions about design modifications to ensure the tension does not exceed the elastic range and the chosen materials are adequate for the operating conditions. Overall, using CFD and FSI analysis can help improve the performance and safety of molten salt heat exchangers.

Consequently, the main research question in this study arises:

"Would there be any permanent damage at the heat exchanger design due to thermal stress ?"

Accordingly, a related sub-question is also identified:

"What is the influence of water pressure on the thermal stress magnitude ?"

Chapter 4

Numerical modelling

This chapter describes the Numerical approach to analyze the thermal stress in a molten salt heat exchanger. The Finite Volume and Finite Element Methods are implemented to obtain these results.

4.1 Model and Mesh generation

Models for simulations were created in the SolidWorks CAD tool and then imported to Ansys Spaceclaim to prepare and select boundary conditions. Meshing is done in the Ansys Fluent Meshing tool. The set of models consists of two cases for molten salt-water heat exchangers. Case 1 (see 4.1):

- Single pipe - representing typical double pipe HX
- $D_{in} = 15.3[mm] D_{out} = 21.3[mm]$
- Lenght of the tube L = 3.7 [m]
- The $\alpha = 1.8\ ^{\circ}$ is the angle at the bend
- The outer walls of the pipe are considered to be fully covered by boiling water and thus convection boundary condition is applied
- Outer side of the pipe is assumed to be fully covered by boiling water

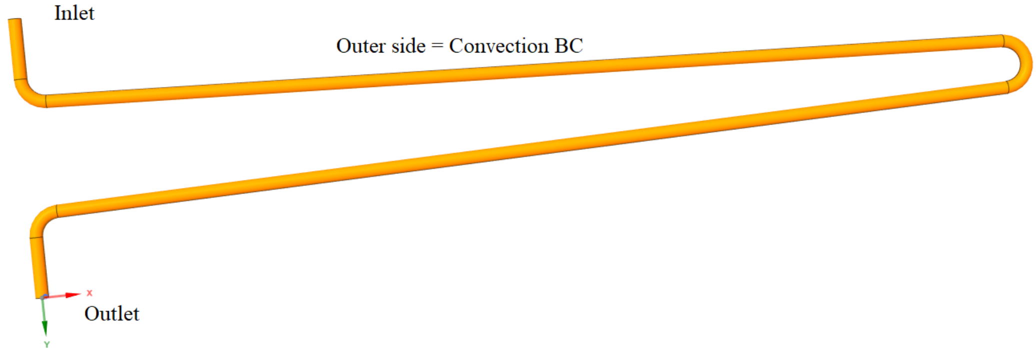

Figure 4.1: Solid domain of single pipe model with BC

The mesh for Case 1 (see 4.2) is created from polyhedral cells. It is typically mentioned that a polyhedral mesh requires fewer cells than tetrahedral. Polyhedral cells indeed introduce fewer problems with regard to cell skewness compare to tetrahedral, as there are made by merging tetrahedral cells. Other advantages typically mentioned for polyhedral cells refer also to the capability of better-representing gradients (because of multiple neighbours) and different flow alignments. Additionally, boundary layers are added to the solid-fluid intersection, because these regions play a significant role in defining the overall fluid dynamics of the problem, and consequently require special attention while simulating the fluid flow.

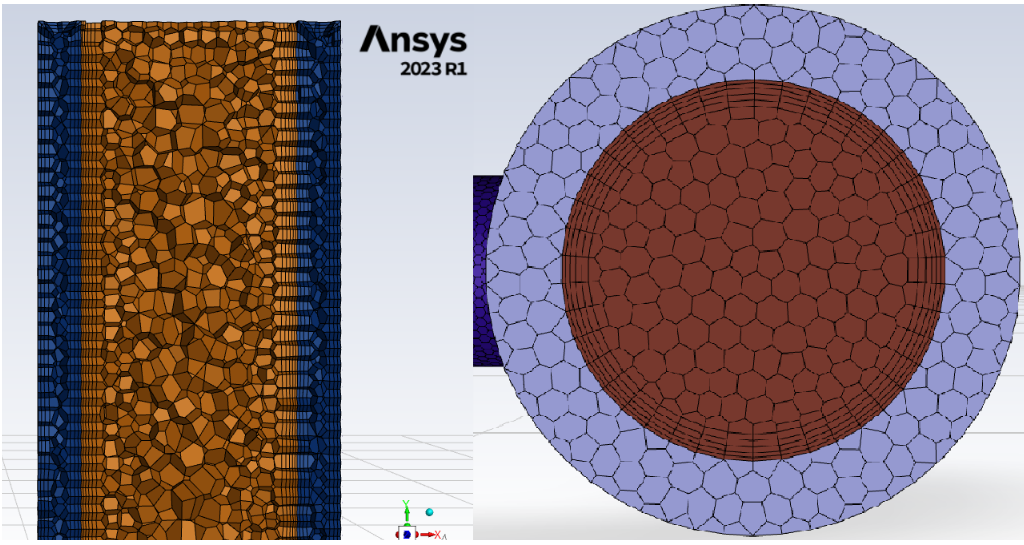

Figure 4.2: Mesh for Case 1, Cross-section of the pipe (left) and Outlet (right)

Case 2 (see 4.3):

- Multiple pipes with manifolds - representing U-tube HX
- $D_{in} = 15[mm] D_{out} = 21[mm]$
- Length of the tubes is L = 3.6 [m]
- Manifolds dimension are $D_{in} = 80[mm] D_{out} = 86[mm]$ L = 300 [mm]
- Pipes are parallel to each other and to the floor
- The pipes are split by plane around the [0,0,0] to divide the area, which is located inside the HX
- The rest of the tubes with manifolds will be considered adiabatic

- The split will be also used in the FSI simulation because the plane is located at the same place where the baffle would be and thus it can serve to define the model and limit the degrees of freedom.

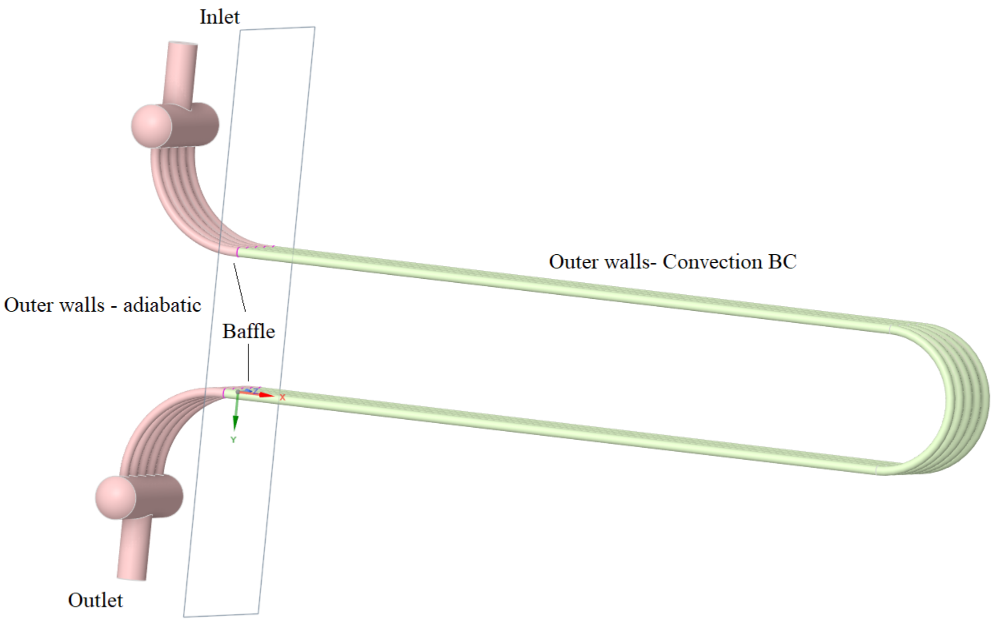

Figure 4.3: Solid domain and boundary conditions of multiple pipes with manifolds model

The mesh for Case 2 (see 4.4) is similar to Case 1 created with the polyhedral method. Also, boundary layers are added to the solid-fluid intersection in the same manner. The mesh for Case 2 consists of 5.1M polyhedral cells with boundary layers at the solid-fluid intersection.

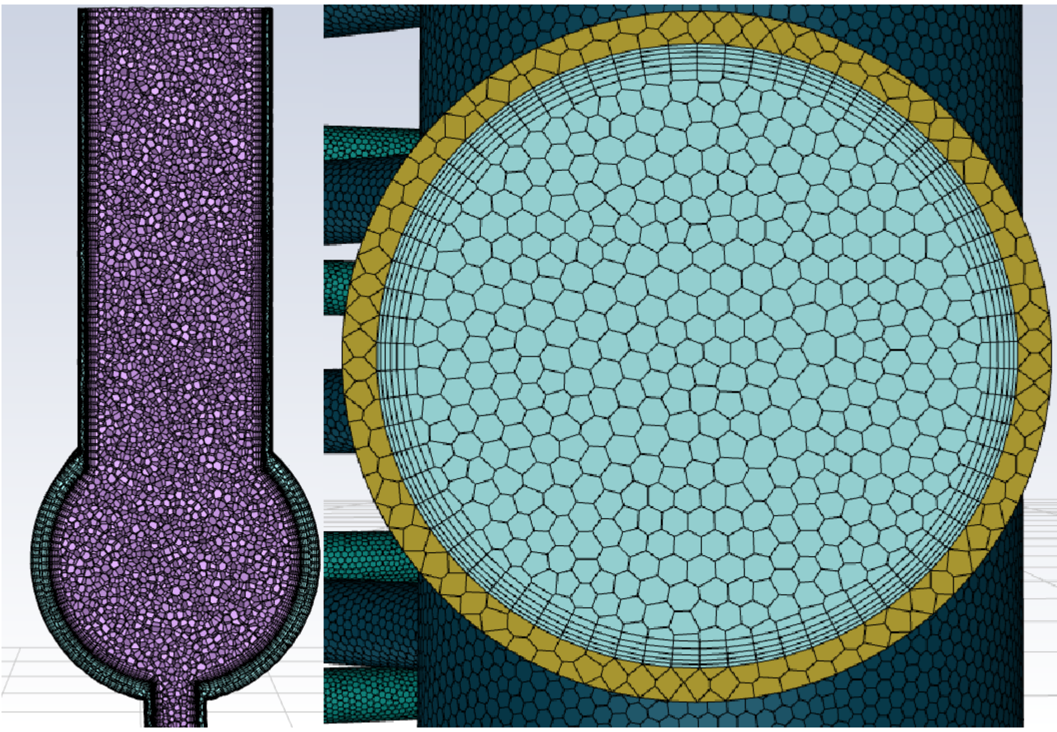

Figure 4.4: Mesh for Case 2, Cross-section of the inlet pipe and manifold (left) and Outlet (right)

It should be mentioned, that it would be possible to use a symmetry plane for the investigated scenarios, which would make the simulations less computationally demanding. However, it is likely that the symmetry plane would suppress some of the physics (e.g. secondary flow in the U-shaped parts).

4.2 CFD setup and boundary conditions

The setup of boundary conditions for Case 1 and Case 2 can be seen in Tab. 4.1. The value of mass flow rate (2.86 $\frac{kg}{s}$) corresponds to a nominal heat rate of 1.2 [MW], if the temperature difference for NaOH ΔT = 200 [K] (for c_p = 2,125 $\frac{W}{kgK}$), which is a planned power output for the facility. This temperature difference is reached in Case 2. The convection boundary condition is described by the Convection heat transfer coefficient and Freestream temperature, which are set up accordingly to simulate the environment in the NaOH-Water HX.

Scenario	Case 1		Case 2	
Inlet	Mass flow [$\frac{kg}{s}$]	Temperature [K]	Mass flow [$\frac{kg}{s}$]	Temperature [K]
	2.86	873.15	2.86	873.15
Outlet	Pressure [Pa]	Temperature [K]	Pressure [Pa]	Temperature [K]
	0 (Gauge)	673.15	0 (Gauge)	673.15
Outer Walls (In HX)	Convection HTC [$\frac{W}{m^2K}$]	FS Temperature [K]	Convection HTC $\frac{W}{m^2K}$	FS Temperature [K]
	5,000	(see Tab.4.5)	5,000	(see Tab.4.5)
Outer Walls (Out HX)	-		Adiabatic	

Table 4.1: Boundary conditions for Case 1 & 2 (HTC = Heat Transfer Coefficient, FS = Freestream)

Investigated Mass flow rate ($\dot{m} = 2.86\frac{kg}{s}$) is equal to Reynolds number = 36,807 for Case 1, which is above the minimum turbulent limit (Turbulent Re > 4000). This also applies to pipes in Case 2, since the inside diameter is similar. Thus, a turbulent turbulence model has to be implemented in the simulation. The SST (Shear Stress Transport) $k - \omega$ is chosen as a turbulence model in this work. SST $k - \omega$ was developed to effectively blend the robust and accurate formulation of the $k - \omega$ model in the near-wall region with the free-stream independence of the $k - \epsilon$ model in the far field. These features make the SST k- ω model more accurate and reliable for a more comprehensive class of flows (e.g., adverse pressure gradient flows, airfoils, transonic shock waves) than the standard k- ω model.

The discretization schemes were chosen as second-order upwind for all parameters. The first-order accuracy discretization schemes are generally considered more stable and yield better convergence, than the second-order, but they typically yield less accurate results. Additionally, the first-order schemes can produce a numerical error generally known as "false diffusion" at simulations, where the flow is not aligned with the mesh (when it crosses the mesh lines obliquely). The setup of the turbulence model and discretization schemes can be seen at Tab.4.2.

Turbulence Model		SST k-w
Disretization Scheme	Pressure	second-order
	Momentum	second-order upwind
	Turbulent kinetic energy	second-order upwind
	Specific dissipation rate	second-order upwind
	Energy	second-order upwind

Table 4.2: Setup of turbulence model and discretization schemes for Case 1 & 2

4.2.1 Conservation equation

In the Reynolds Averaging Navier-Stokes (RANS) equation, the variables are decomposed into the mean (ensemble-averaged or time-averaged) and fluctuating components.

For the velocity components:

$$u_i = \overline{u_i} + u_i' \tag{4.1}$$

where $\overline{u_i}$ and u_i' are the mean and fluctuating velocity components (i = 1, 2, 3).

Likewise, for pressure and other scalar quantities:

$$\phi = \overline{\phi} + \phi' \tag{4.2}$$

where ϕ denotes a scalar such as pressure or energy.

The equation for conservation of mass or continuity equation used by Ansys Fluent for incompressible flow can be written as follows:

$$\frac{\partial}{\partial x_i}(\overline{u_i}) = 0 \tag{4.3}$$

where ρ is density, t is time and $\overline{u_i}$ is velocity
Conservation of momentum in an inertial or non-accelerating reference frame can be then defined as:

$$\frac{\partial}{\partial x_j}(\rho\overline{u_i u_j}) = -\frac{\partial p_i}{\partial x_i} + \frac{\partial}{\partial x_j}[(\mu + \mu_t)(\frac{\partial \overline{u_i}}{\partial x_j} + \frac{\partial \overline{u_j}}{\partial x_i}] \tag{4.4}$$

where p_i is static pressure and μ is dynamic viscosity

Equations 4.3 and 4.4 Reynolds-averaged Navier-Stokes (RANS) equations. They have the same general form as the instantaneous Navier-Stokes equations, with the velocities and other solution variables now representing ensemble-averaged (or time-averaged) values. Additional terms now appear that represent the effects of turbulence.

Ansys Fluent solves the energy equation in the following form:

$$\nabla \cdot (\rho\overline{u_i}(h + \frac{\overline{u_i}^2}{2})) = \nabla \cdot (k_t \nabla T + \tau_t \cdot \overline{u_i}) \tag{4.5}$$

where k_t is the turbulent thermal conductivity, defined according to the turbulence model being used). The two terms on the right-hand side of the Equation represent energy transfer due to conduction, and viscous dissipation, respectively.

In solid regions, the energy transport equation used by Ansys Fluent has the following form:

$$\nabla \cdot (\overline{u_i}\rho h) = \nabla \cdot (k\nabla T) \tag{4.6}$$

where k is conductivity, T is temperature and h is a sensible enthalpy solved by Eq. 4.7

$$h = \int_{T_{ref}}^{T} c_p dT \tag{4.7}$$

4.2.2 Turbulence model

The turbulence model is a two-equation model that solves transport equations for the turbulent kinetic energy and the turbulent dissipation rate to determine the turbulent eddy viscosity. The SST model incorporates a damped cross-diffusion derivative term in the ω equation. The definition of the turbulent viscosity is modified to account for the transport of the turbulent shear stress and the modelling constant is different. The model consists of three equations, namely the turbulence-specific dissipation rate equation (Eq. 4.8), the turbulence kinetic energy equation (Eq. 4.9) and The turbulence viscosity equation (Eq. 4.10).

The turbulence-specific dissipation rate and the turbulence kinetic energy is given by:

$$\frac{\partial}{\partial x_i}(\rho\omega u_i) = \frac{\partial}{\partial x_j}(\Gamma_\omega \frac{\partial \omega}{\partial x_j}) + G_\omega - Y_\omega \tag{4.8}$$

$$\frac{\partial}{\partial x_i}(\rho k u_i) = \frac{\partial}{\partial x_j}(\Gamma_k \frac{\partial k}{\partial x_j}) + G_k - Y_k \tag{4.9}$$

where ω is the specific dissipation rate, k is the turbulence kinetic energy, G_k represents the generation of turbulence kinetic energy due to mean velocity gradients, G_ω represents the generation of the specific dissipation rate, Γ_k and Γ_ω represent the effective diffusivity of k and ω, respectively, Y_k and Y_ω represent the dissipation of k and ω, due to turbulence.

The turbulent viscosity μ_t is computed by combining k and ω as follows:

$$\mu_t = \frac{\rho k}{\omega} \tag{4.10}$$

4.2.3 Material properties

The investigated scenario consists of the following fluids: water and molten sodium hydroxide. Water is replaced in the simulation by convection boundary conditions for the outer side of the pipe walls, which corresponds to the heat transfer coefficient and temperature of forced convection by boiling water. The temperature-dependent thermophysical properties for NaOH used in the simulation have been provided by an external organization and are bound by a non-disclosure agreement and thus can not be published. Thermophysical properties of the NaOH with a publicly accessible reference can be seen in Tab.4.3. As has been previously stated, due to the corrosivity of the molten NaOH or molten salts. Materials with high resistance against corrosion need to be chosen for the heat exchanger. Nickel-alloy Inconel 600 is considered in this study as a material for the solid domain as it shows great durability against corrosion even under high temperatures. Thermophysical properties of the Inconel 600 were taken from GRANTA MDS Database and can be seen in Fig.4.5.

Material	Density [$\frac{kg}{m^3}$]	Specific heat capacity [$\frac{kJ}{kgK}$]	Thermal conductivity [$\frac{W}{mK}$]	Viscosity [$Pa \cdot s$]	Melting Point [K]
NaOH (at 400°C)	1750	2.26	1.08	0.0207	591.15

Table 4.3: Thermal properties of the sodium hydroxide [9]

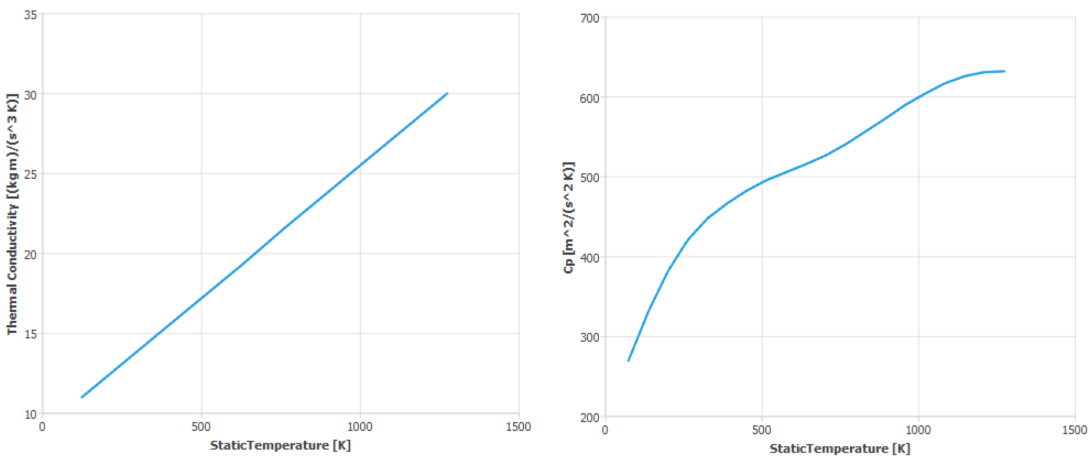

Figure 4.5: Thermal properties of the Nickel-Alloy Inconel 600

4.3 Grid independency analysis

To ensure the accuracy and credibility of CFD predictions a mesh independency study is performed to ensure that all important flow phenomenon is resolved in the simulation, due to the coarseness of the mesh. Because of the limited time, only the scenario with a single pipe will be investigated.

Inlet	Mass flow inlet [$\frac{kg}{s}$]	2.86
	Inlet temperature [K]	873.15
Outlet	Pressure Outlet [Pa]	0 (Gauge)
	Backflow temperature [K]	673.15
Wall - Convection BC	Convection heat transfer coefficient [$\frac{W}{m^2K}$]	5,000
	Freestream temperature [K]	373.15

Table 4.4: Boundary conditions for grid independency analysis

The simulation is set up accordingly to Tab.4.4. The domain consists of the solid and fluid domains. The fluid domain is filled by molten Sodium Hydroxide. The material of the solid domain is Nickel Alloy Inconel 600. The analysis will consist of 6 different mesh densities and the key parameter for comparison will be overall heat flux.

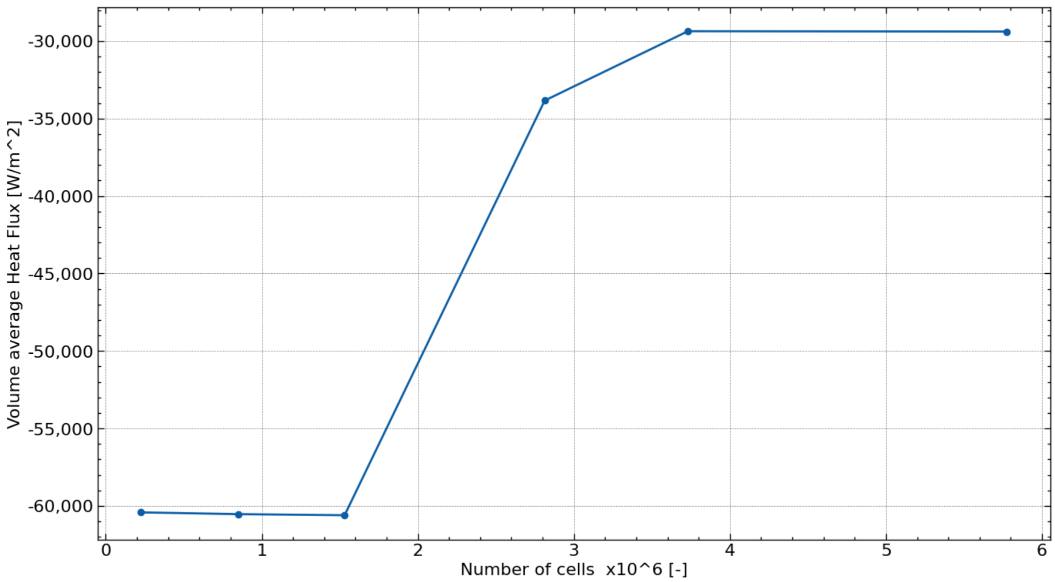

Figure 4.6: CFD Grid independency analysis for Case 1

As the graph 4.6 shows, the value for overall heat flux was close to -60,000 $\frac{W}{m^2K}$ for the first three coarser meshes and with finer mesh the value increased to approximately -30,000 $\frac{W}{m^2K}$. Thus the meshes with a number of cells less than 3 million do not capture the behaviour of the flow properly and the mesh with 3.7M cells is chosen for the simulation as there is minimal difference between the two finest meshes. The sudden increase of almost 100% in Overall Heat Flux seems strange and one can only speculate on the reasons behind it. One of the reasons could be due to the insufficient number of cells in the solid domain, where there would be only one cell in the thickness.

In an identical manner, the grid independency analysis is also performed for the FEM analysis, where the investigated volume consists solely of the solid domain. The results of CFD analysis from the 3M number of cells grid are imported to the Ansys mechanical, where the new mesh is generated and the temperature map is imported. The FEM simulation for Von Mises stress is then initialized and the simulation results for different mesh coarseness are compared (see 4.7).

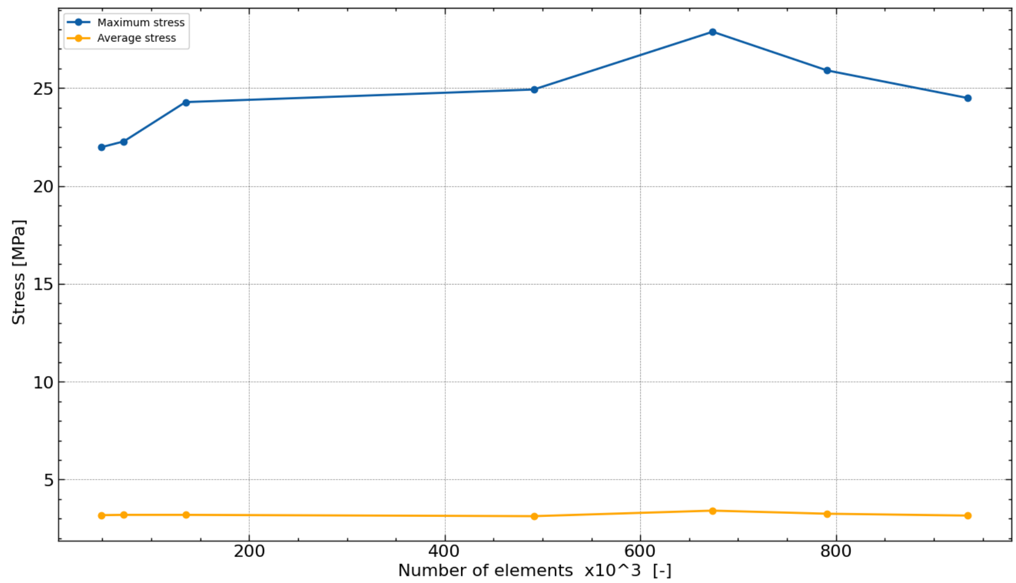

Figure 4.7: FEM grid independency analysis for Case 1

The comparison between grids is made through Maximum stress and Average stress. As can be seen, the average stress results are very similar for most grids with only a noticeable peak at 674K number of elements, which corresponds to the peak of maximum stress level. The two finest meshes (791K & 935K) produce identical results for the average and maximum stress, the differences are at the acceptable level and the grid with 791K number of elements can be considered sufficient. The results will be later shown in Section 5.1.1

4.4 Simulation matrix

According to the problem statement and the research questions. The simulation matrix is created (see Tab.4.5). Case 1 and Case 2 are simulated with variations in the freestream temperature for convection boundary conditions. This parameter directly corresponds to the statement that the pipes of the heat exchanger are surrounded by boiling water. Since the temperature of the boiling point is pressure-dependent the freestream temperature will increase with the pressure of the water. According to [22], the common pressure of the working fluid at water-water heat exchangers varies between 1.4 to 7 [bar] and regarding the thermal power plant the water can reach pressure in the order of 100[bar] in the boiler. On the other hand, with the increasing pressure of the working or heat transfer fluids, the design of the heat exchanger becomes more expensive as there are additional requirements for sealing and the pumps in the system. Thus, the range for investigation of thermal stress is set starting with 1 bar as a reference pressure, because the boiling point temperature is lower and is expected to produce the highest stress, the rest of the pressure is chosen between the range published by IBM.

Scenario	Water pressure [bar]	Boiling point Temp. [K]
Case 1	1	373.15
	2	393.35
	5	425.05
Case 2	1	373.15
	2	393.35
	5	425.05

Table 4.5: Simulation matrix for Case 1 & Case 2

4.5 Validation case

To support the reliability of numerical modelling, validation of results with experimental or analytical studies need to be made. Although CFD is a great tool to predict flow behaviour, a detailed assessment of errors and uncertainties has to be made. Validation has also been described as "solving the right equations". The strategy is to identify and quantify error and uncertainty by comparing simulation results with experimental data.

Since this study is mainly concerned with the correct prediction of the distribution of thermal stress, the validation of the setup is performed in a case where the dominant mechanism causing thermal gradient in the solid region is the conduction of the hot and cold instead of thermal gradients induced by different temperatures of internal and external flow. The investigated case [23]was dealing with thermal mixing in a T-junction with the cold and hot streams (see Fig.4.8). The fluid material was water and the material of the solid domain was structural steel, both available in the Ansys material database. The comparison of the results is done in two stages first the results of CFD analysis will compare the temperature distribution with the experimental and simulation data from [24]. In the second stage, the results of the thermal stress analysis performed in Ansys Mechanical will be compared to the investigated case.

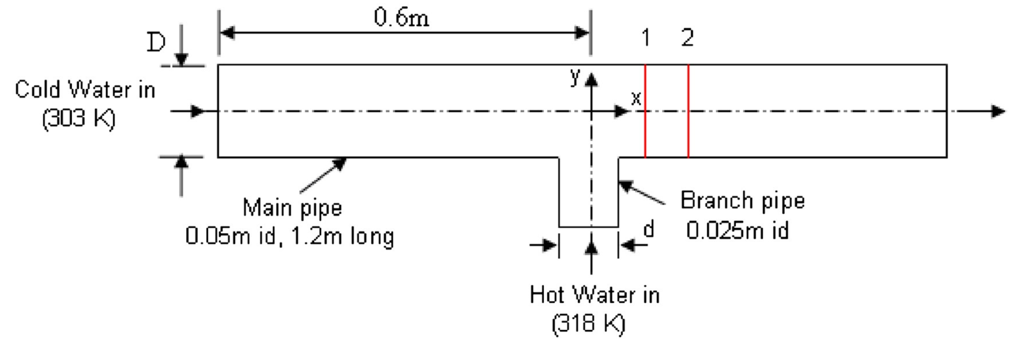

Figure 4.8: T-junction for validation case with dimensions and temperatures of the streams, Line 1 and 2 represents locations of temperature probes [23]

The results from CFD analysis are extracted in the form of a temperature profile at line 1 and compared to the experimental data in Fig.4.9. The y-axis is represented by the rate between the y-position on the line and the radius of the main pipe. The x-axis is represented by the normalized temperature can be calculated as follows:

$$T_{norm} = \frac{T - T_C}{T_h - T_c} \tag{4.11}$$

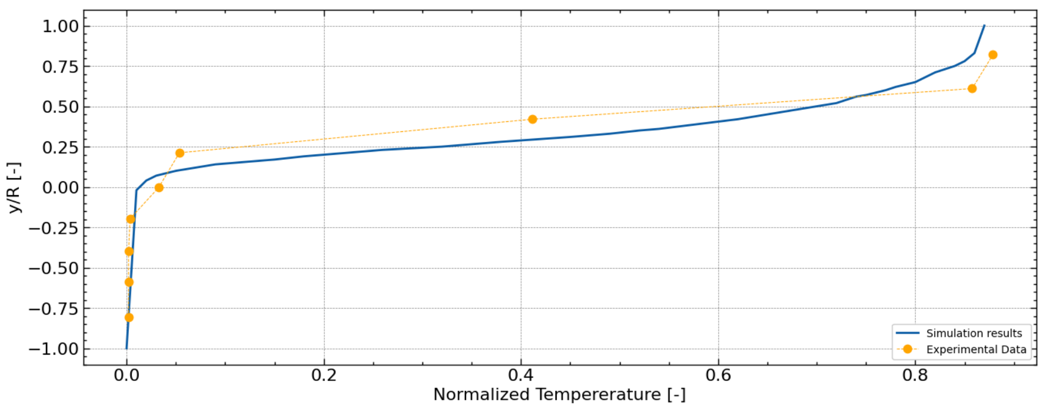

Figure 4.9: Comprasion of CFD simulation and experimental data from Line 1

As can be seen, the prediction of temperature distribution is captured properly and is in good agreement with the experimental data. It can be observed that there is an offset in the zone from y/R = 0 to 0.6. This could be caused by the mixing and secondary flow induced by turbulence, which is very difficult to capture correctly with CFD simulation, especially in a steady state with k-ω or $k - \epsilon$ turbulence models. The simulation results could be improved by changing the turbulence model to Detached Eddy Simulation (DES) or Large Eddy Simulation (LES). However, these turbulence models do not allow steady-state simulation and would be computationally expensive. Moreover, it should be mentioned that the experimental data are not available in the full range of Line 1. Additionally, the temperature-measuring devices have a certain level of uncertainty, which could add to the differences between the experimental and simulation data. Considering everything above, the differences between the experiment and simulation can be considered negligible and the CFD setup can be considered validated.

Due to a distinct lack of experimental data in the available literature concerning the thermal stress analysis within the pipework, the thermal stress analysis comparison will be done with simulation results from a previously mentioned study. The model together with the results of CFD simulation are therefore imported to Ansys Mechanical for Thermal stress analysis (TSA). In order to perform TSA the boundary conditions needs to be set to limit the degrees of freedom. This is done in the form of remote displacement BC at the inlet face, which corresponds to the end of the mixing tee pipe being fixed in space.

As can be seen in Fig. 4.10, the thermal stress beyond the mixing point has a magnitude between 5 - 15 MPa. As expected, the highest stress occurs in the area around the connection between the main and branch pipe. These values can be explained as this is the area where the hot and cold flow starts mixing and the thermal gradients are highest.

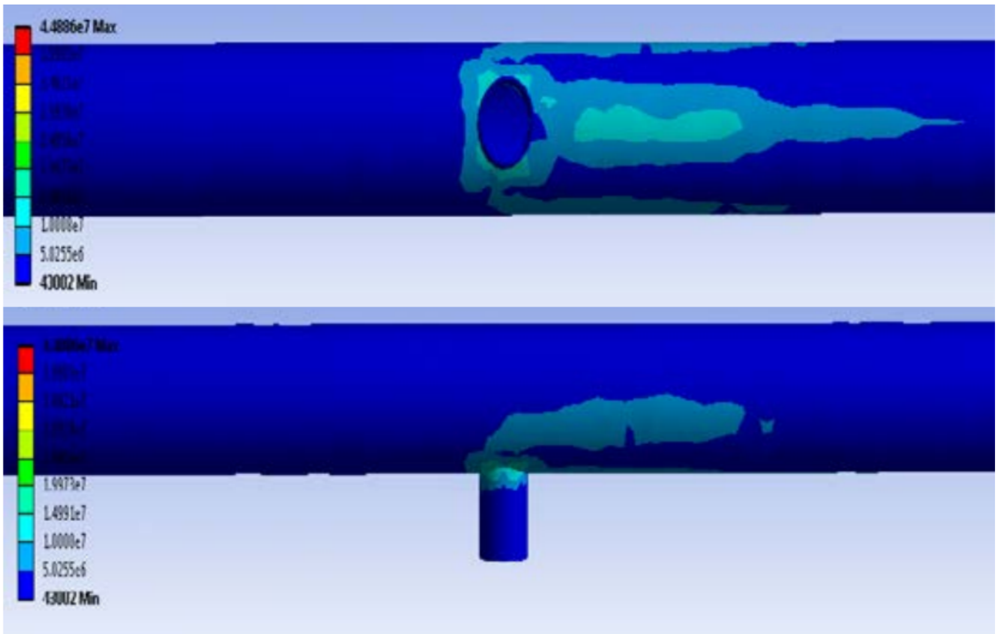

Figure 4.10: Contours of Von Misses stress at XZ and YZ plane of the investigated case [23]

While the validation case results in different contours of the thermal stress (see 4.11). It can be observed that the magnitude of the stress is similar and in the same range as the investigated study. This can be explained by different used turbulence models, which resulted in a variance of the turbulence eddies and thus in different locations of the temperature gradients, which produced two different contours of the thermal stress. Moreover, it should be mentioned that the mesh used in this study is much finer in comparison with the investigated case.

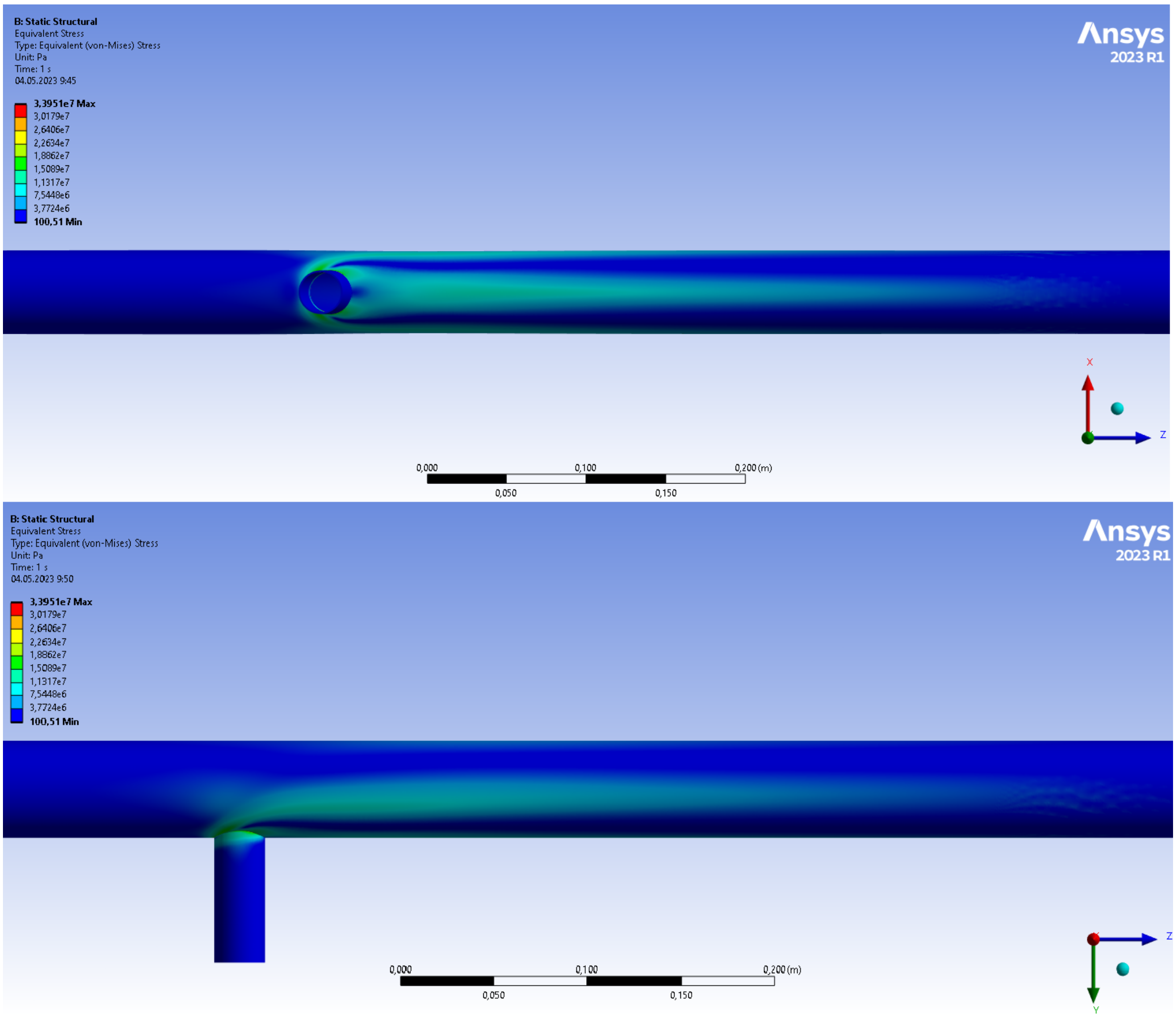

Figure 4.11: Contours of Von Misses stress at XZ and YZ plane of the validation case

Even though, the contours of Von Mises stress are not identical. The stress range for both cases is similar and because this study is mainly interested in the correct capture of the magnitude of thermal stress and the risk of fatigue damage. Although, the results of the analysis should be later verified by experiment.

4.6 Fluid-Structure Interaction setup and boundary conditions

After the CFD simulations, the temperature field is imported into Ansys Mechanical for thermal stress analysis of the solid model. Boundary Conditions or Supports are an important part of the FEM analysis setup as they allow users to define parts, which are not present in the model but are interacting with it. Supports help simplify the domain, which helps in efficiently obtaining numerically accurate results without modelling parts of the geometry that are not of primary interest. Moreover, supports are used to constrain the model in space and thus limit the degrees of freedom. There are different types of support available, and choosing the appropriate support is essential as it assures that the simulation model will properly represent the boundary condition.

The supports used in investigated cases can be seen in Tab.4.6. Remote Displacement Support (RDS) was used for both cases as it allows the investigation of thermal stress with disregarding the stress due to constrained expansion. For Case 1, the position of the support was the Inlet of the tube, due to the assumption that there would be a flange connected to the pump. For Case 2, the position of the support was chosen as the expected location of the baffle. Since the Remote Displacement Boundary conditions do not take into account stress induced by constrained expansion, one more set of simulations for Case 2 is performed with Fixed Support where all translation movement is 0. This simulation is supposed to represent the situation, where the baffle is pressed on the pipes. Although, in real applications, there would be some sort of sealing to prevent a leak, which would also serve as elastic support and the expansion of the pipe would just pressure the sealing and absorb the majority of the stress. However, it is important to note that the level of support provided by the sealing would depend on its material properties and the amount of expansion that occurs. Therefore, while sealing may help to mitigate the stresses induced by thermal expansion, it may not completely eliminate them.

Scenario		Case 1	Case 2	
Position		Inlet	Baffle	
Support Type		RDS	RDS	Fixed Support
Displacement	x [m]	0	0	0
	y [m]	0	0	0
	z [m]	0	0	0
	R_x [°]	0	0	0
	R_y [°]	0	0	0
	R_z [°]	0	0	0

Table 4.6: Boundary conditions for FEM analysis

4.6.1 Governing equations

Most metals expand with heat, and the metal structure will produce deformations if there is no space to expand. The structures are generally constrained from other structures and themselves, this will lead to thermal deformation and thermal stress. Thermal strain induced in 1-D rod can be calculated by following Eq.4.12

$$\varepsilon_0 = \alpha \Delta T \tag{4.12}$$

where α is the coefficient of thermal expansion, ΔT is the change of temperature e.g. $(T - T_{ref})$

$$\{\sigma\} = [D] \cdot (\vec{\varepsilon} - \vec{\varepsilon_0}) \tag{4.13}$$

where $[D]$ is the elastic matrix, and $\vec{\varepsilon_0}$ is the thermal strain which denotes deformations caused by temperature.

The elastic matrix represents the stiffness matrix of an elastic material. It is a mathematical representation of the relationship between the applied forces and the resulting deformations of a solid material. It contains the elastic constants of the material, which are typically the Young's modulus, the Poisson's ratio, and the shear modulus. It can be calculated as follows:

$$[D]\vec{u} = \vec{F} \tag{4.14}$$

where $\vec{u}$ is the vector of nodal displacements, and $\vec{F}$ is the vector of nodal forces.

The total strain ε in the Eq.4.13 is calculated by the following equation in FEM analysis:

$$\vec{\varepsilon} = [B] \cdot \vec{\delta}^e \tag{4.15}$$

where $[B]$ is the stain matrix and δ^e is the nodal displacement which can be obtained by solving the equation as follows:

$$[K] \cdot \vec{\delta} = \vec{Q}_T \tag{4.16}$$

where $[K]$ is the stiffness matrix and Q_T is the thermal load.

The stiffness matrix represents the stiffness properties of an elastic material. It is derived based on the geometry, material properties, and boundary conditions of the analyzed structure. It is used to solve for the nodal displacements and nodal forces and is calculated in the FEM tools as follows:

$$[K] = \int (B^T[C]B)dV \tag{4.17}$$

$[C]$ is the constitutive matrix that relates the stress and strain, and dV is the element volume.

Chapter 5

Results and Discussion

The results of the CFD simulations are compared in the form of temperature contours. As has been said in the previous chapter, a set of 6 coupled CFD-FEM simulations was done for different pressure of the working fluid for Case 1 & Case 2. CFD simulations were run in steady-state until "Machine Accuracy" has been reached. The comparison of the FEM simulations was done through contours of Von Mises stress. Moreover, maximal stress and his position have been written for comparison and calculation of the Factor of Safety, which will be introduced later in this section.

5.1 Case 1 - pipe-in-pipe Heat exchanger

5.1.1 Scenario with the pressure of working fluid 1 bar

As has been previously stated, the scenario with atmospheric pressure serves as a reference case, because it is expected to produce the highest temperature gradient and thus the largest thermal stress. Temperature contours of a cross-section of a pipe for Case 1 can be seen in Fig.5.1. The border of solid (Inconel 600) and fluid (molten NaOH) is divided by a black circle. It can be seen that the main temperature gradient is in the solid part and the temperature gradient in the fluid is much smaller due to convection heat transfer and turbulent mixing in the fluid. This is expected to cause thermal stress due to the differential expansion and contraction of the pipe material due to the temperature gradient across its cross-section.

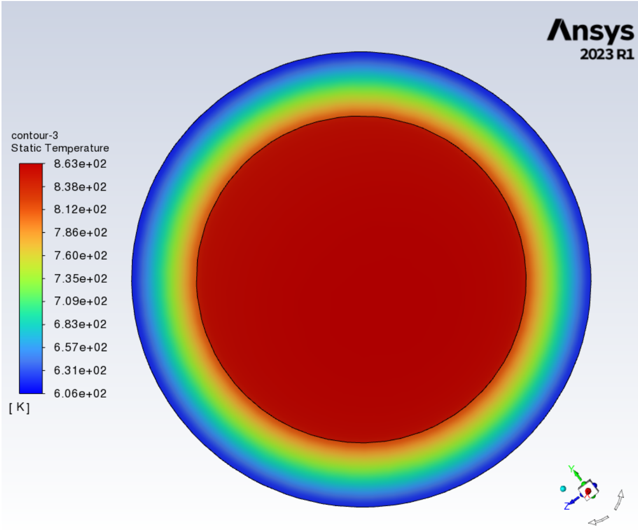

Figure 5.1: Temperature Contours of a cross-section of pipe for Case 1 - 1 [bar], solid and fluid domain is divided by a black circle

The temperature contours of an inner wall can be seen in Fig.5.2. As expected the temperature across the length of the pipe is decreasing, due to the constant heating of the surrounding water. There are clearly visible temperature gradients at both the elbows and at the U-shape part of the pipe. This can be explained by a sudden change in the direction of the flow, which results in a centrifugal force that causes the fluid to move towards the outer wall of the elbow. This centrifugal force creates a secondary flow, known as a "secondary flow circulation," which further contributes to the mixing of the fluid and the development of temperature gradients.

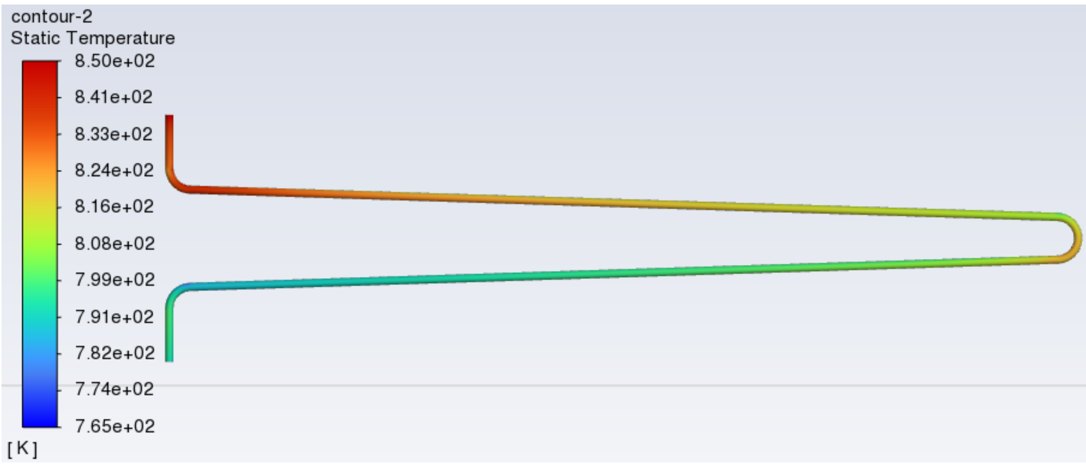

Figure 5.2: Temperature Contours of an inner wall of pipe for Case 1 - 1 [bar]

The contours of Von Mises stress can be seen in Fig. 5.3. Due to the previously discovered temperature gradients at the U-shape part and the elbows, these locations are selected for mesh refinement to produce a more realistic contour map. Additionally, the maximal stress occurs at the elbow located below the inlet. This is due to the temperature decreasing farther from the inlet and thus the thermal gradients, caused by circulation are decreasing, at the other bent parts. One of the mechanisms, which creates stress in the pipe, could be the secondary flow circulation in the bents of the pipe. Another, parameter influencing the location of increased stresses could be the geometry of the bend.

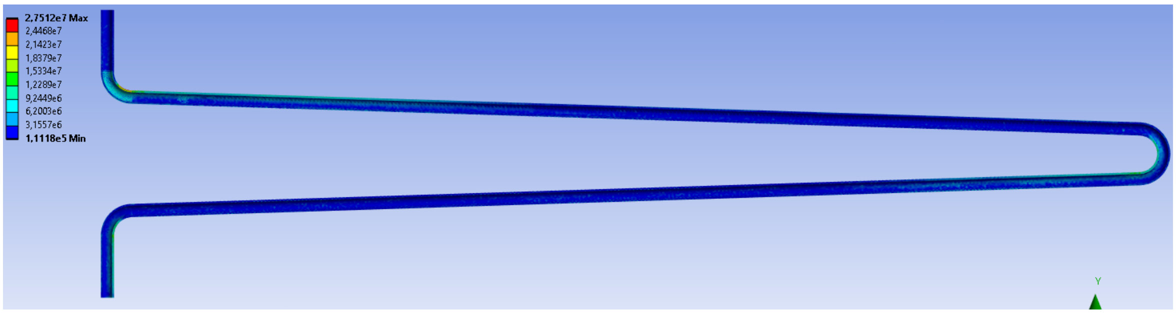

Figure 5.3: Contours of Von Mises stress of pipe for Case 1 - 1 [bar] with a Remote Displacement Support, the pipe is cut in x=0 plane for better visibility of stress distribution in the pipe and in the material thickness

The detail on a cut of the inlet elbow can be seen in Fig.5.4 together with the comparison of temperature and stress contours. It can be clearly seen that the temperature gradients are corresponding to the locations of the stress. The maximum stress for this scenario is thus 27.5 [MPa] with the location at the outer side of the small radius of the inlet elbow.

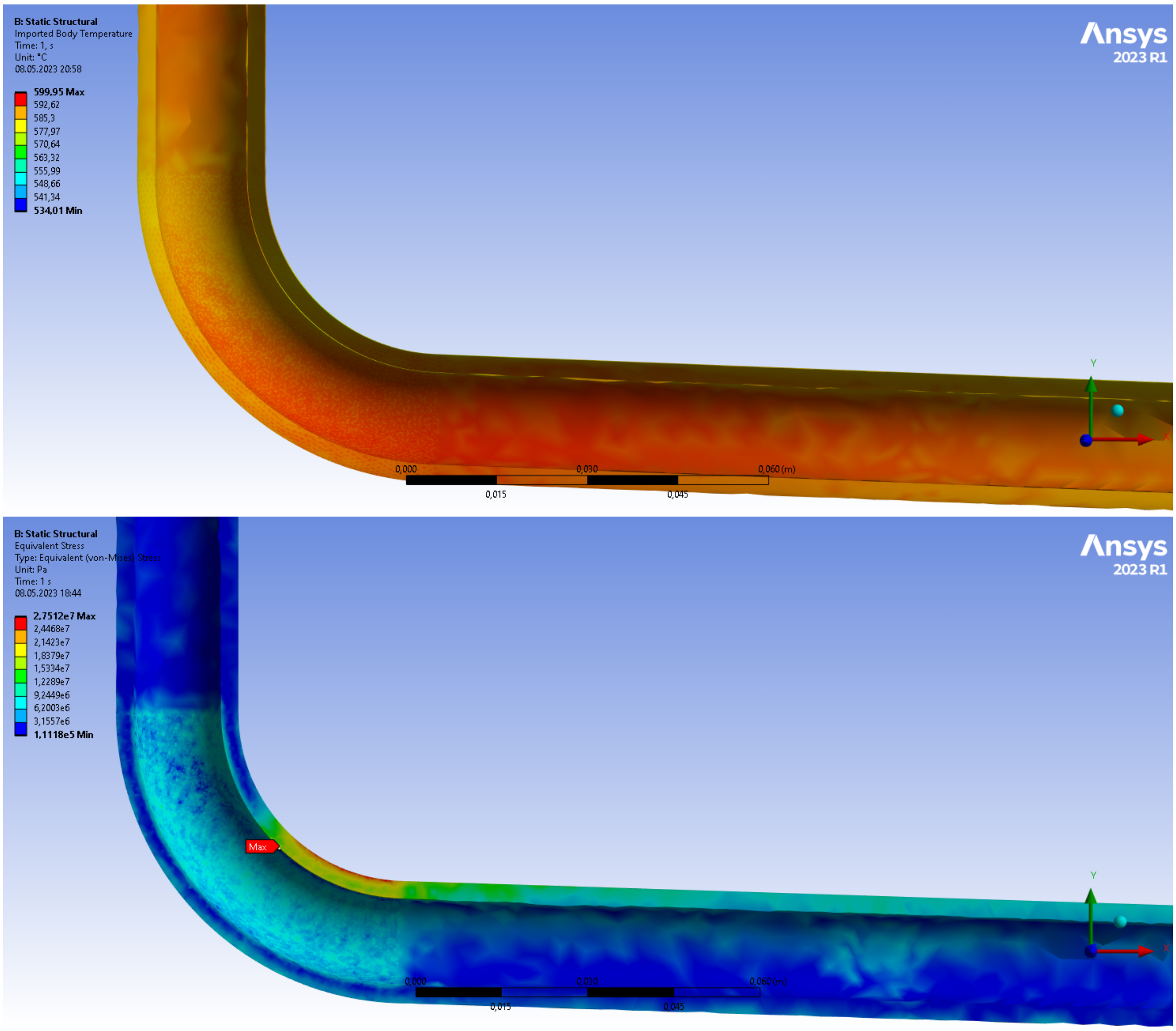

Figure 5.4: Contours of Temperature (upper) and Von Mises stress (lower) of the inlet elbow for Case 1 - 1 [bar] with Remote Displacement Support

5.1.2 Scenario with the pressure of working fluid 2 bar

As the pressure of water increase, the temperature of the boiling point increase with it. So at the pressure of 2 [bar] the boiling point reaches the temperature of 393.35 [K]. The temperature contours of a cross-section of the pipe can be seen in Fig.5.5. In comparison with the previous scenario, the temperature distribution is similar with a different minimum temperature, which is caused by higher freestream temperature in the convection boundary condition. The border of solid (Inconel 600) and fluid (molten NaOH) is divided by a black circle. The effect of external and internal convection heat transfer can be seen, as the hot fluid is heating up the pipe from the inside, while the cold fluid is cooling it from the outside. This is expected to cause thermal stress due to the differential expansion and contraction of the pipe material due to the temperature gradient across its cross-section.

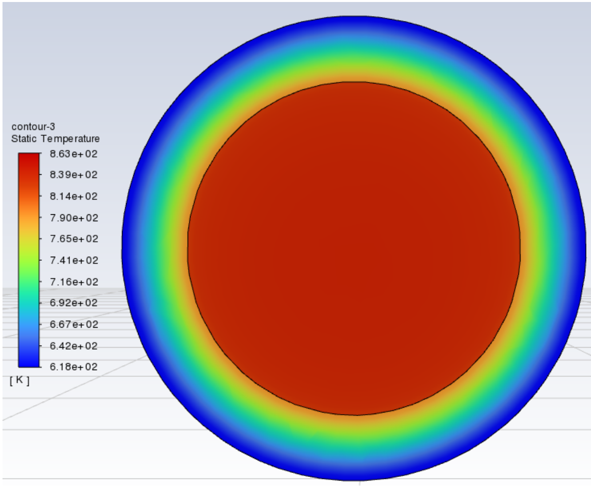

Figure 5.5: Temperature Contours of a cross-section of pipe for Case 1 - 2 [bar], solid and fluid domain is divided by a black circle

As can be seen in Fig.5.6, the temperature distribution around the inner walls of the pipe displays similar behaviour as in the previous case. The elbow and the U-shape part of the pipe are causing a sudden change in the direction of the flow, which is causing temperature gradients due to flow circulation as in the previous scenario.

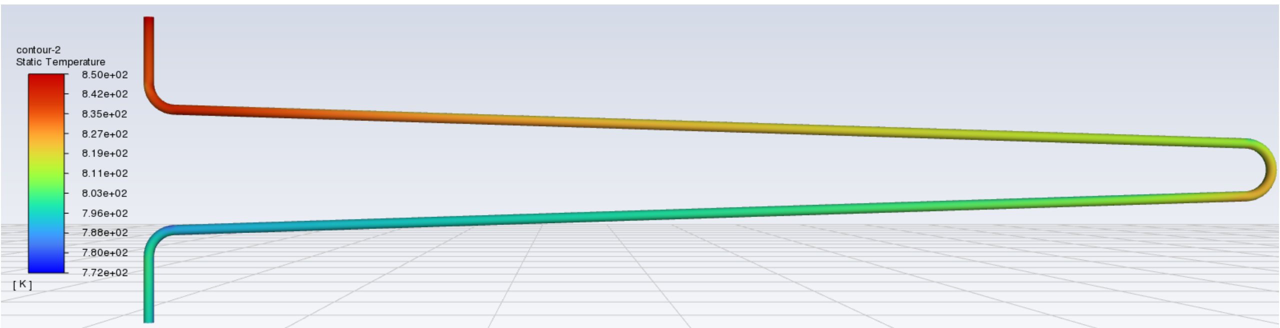

Figure 5.6: Temperature Contours of an inner wall of pipe for Case 1 - 2 [bar]

Contours of Von Mises stress for Case 1 - 2 [bar] (see Fig.5.7) are in good agreement with the Temperature Contours, as the locations of higher stress appear in the elbows and U-shape. Moreover, it can be seen that the turbulent mixing caused by a sudden change in flow direction continues to create thermal gradients and thus thermal stress after the elbows and also after the U-shape.

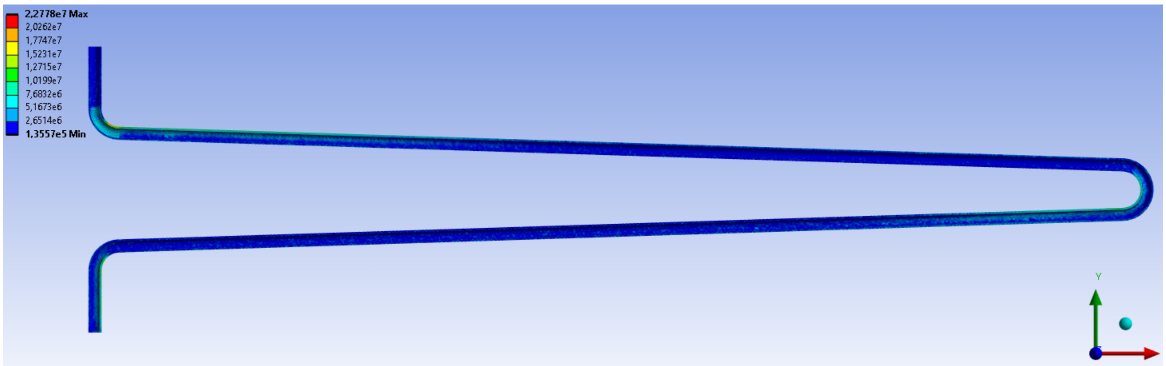

Figure 5.7: Contours of Von Mises stress for Case 1 - 2 [bar], the pipe is cut in x=0 plane for better visibility of stress distribution in the pipe and in the material thickness

The Comparison between the temperature map and Von Mises stress at the locations of maximum stress can be seen in Fig.5.8. The location of the maximal stress is a cut of the inlet elbow same as in the previous scenario. The maximal stress for Case 1 - 2 [bar] is 22.8 [MPa].

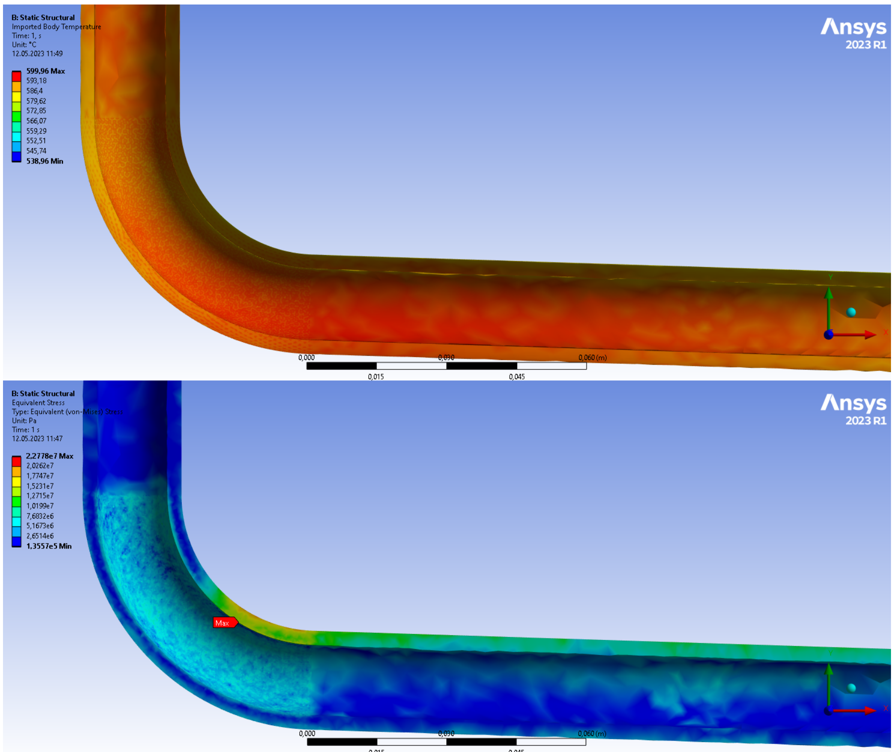

Figure 5.8: Contours of Temperature (upper) and Von Mises stress (lower) of the inlet elbow for Case 1 - 2 [bar]

5.1.3 Scenario with the pressure of working fluid 5 bar

The temperature of the boiling point for pressurized water at 5 [bar] is equal to 425.05 [K]. The temperature contours of a cross-section of the pipe can be seen in Fig.5.5. The border of solid (Inconel 600) and fluid (molten NaOH) is divided by a black circle. The minimal temperature at the cross-section is higher than for the previous cases, which is caused by the higher temperature of the surrounding water. This is expected to create fewer temperature gradients and therefore lower thermal stress, due to different expansions across the thickness of the pipe.

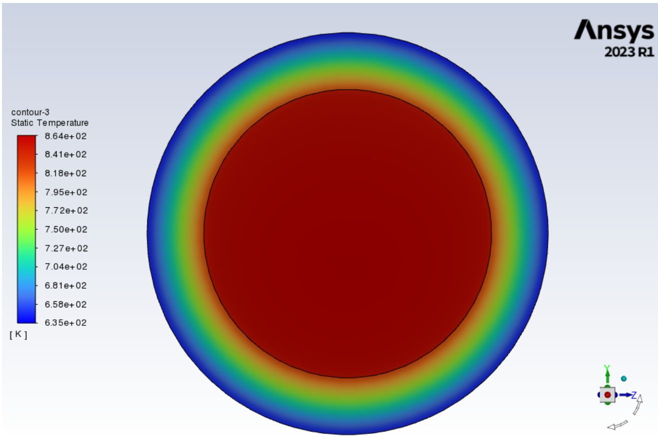

Figure 5.9: Temperature Contours of a cross-section of pipe for Case 1 - 5 [bar], solid and fluid domain is divided by a black circle

The temperature contours of the inner wall of the pipe can be seen in Fig.5.10. The temperature distribution is showing a similar trend as the previous cases with a small difference in temperature magnitude and minimal temperature. This is caused by the increased pressure of the water, which results in a higher temperature of the surrounding boiling water.

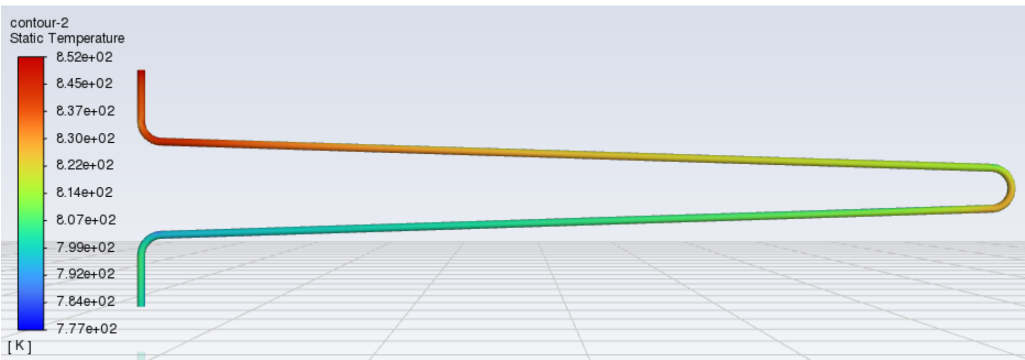

Figure 5.10: Temperature Contours of an inner wall of pipe for Case 1 - 5 [bar]

The stress distribution along the pipe can be seen in Fig.5.11 in the form of Von Mises stress contours. As expected, the stress contours are similar to the previous cases with a decreased magnitude of the stress.

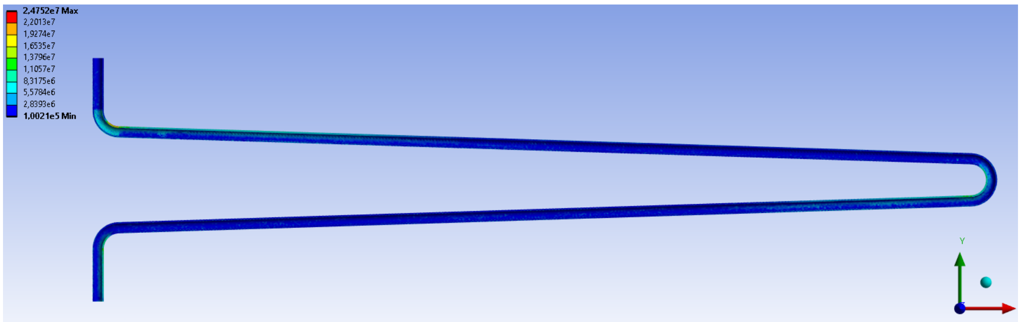

Figure 5.11: Contours of Von Mises stress for Case 1 - 5 [bar], the pipe is cut in x=0 plane for better visibility of stress distribution in the pipe and in the material thickness

The maximum stress is located at the inlet elbow as in the previous scenarios. The distribution and the magnitude of the stress together in comparison with the temperature map of the inlet elbow can be seen in Fig.5.12. The maximum stress of Case 1 with water pressure 5 [bar] is located at the outer wall of the small radius in the inlet elbow and has a magnitude of 24.8[MPa].

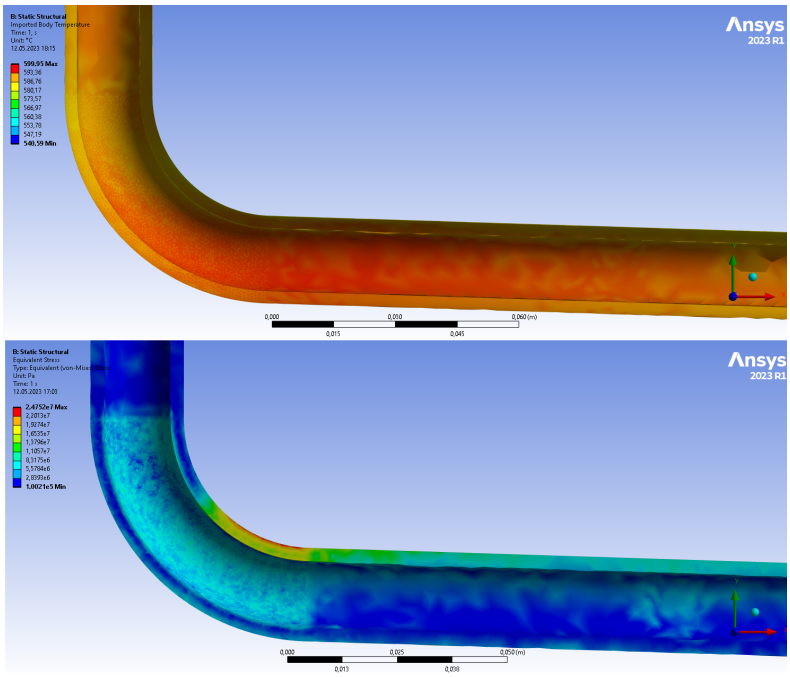

Figure 5.12: Contours of Temperature (upper) and Von Mises stress (lower) of the inlet elbow for Case 1 - 5 [bar]

5.2 Case 2 - U-tube Heat exchanger

5.2.1 Scenario with the pressure of working fluid - 1 [bar]

The temperature contours of a cross-section of the centre pipe of Case 2 can be seen in Fig.5.13. Similarly, as for the first case, there are noticeable temperature gradients happening across the thickness of the pipe, caused by the temperature difference between cold and hot streams.

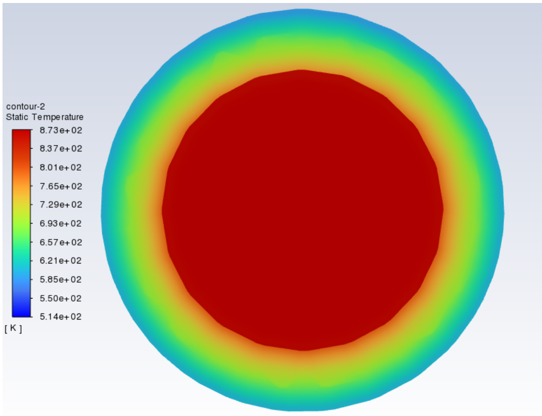

Figure 5.13: Temperature Contours of a cross-section of pipe for Case 2 - 1 [bar]

The contours of temperature for Case 2 with atmospheric pressure can be seen in Fig.5.14. Since the convection boundary condition has not been applied to the whole surface of the model, but rather to the parts of the pipes, which would be actually inside the drum of the heat exchanger, the temperature of the walls outside of the drum is similar to the temperature of the molten Sodium Hydroxide. There can be seen high-temperature gradients happening at the borders of the convection boundary condition.

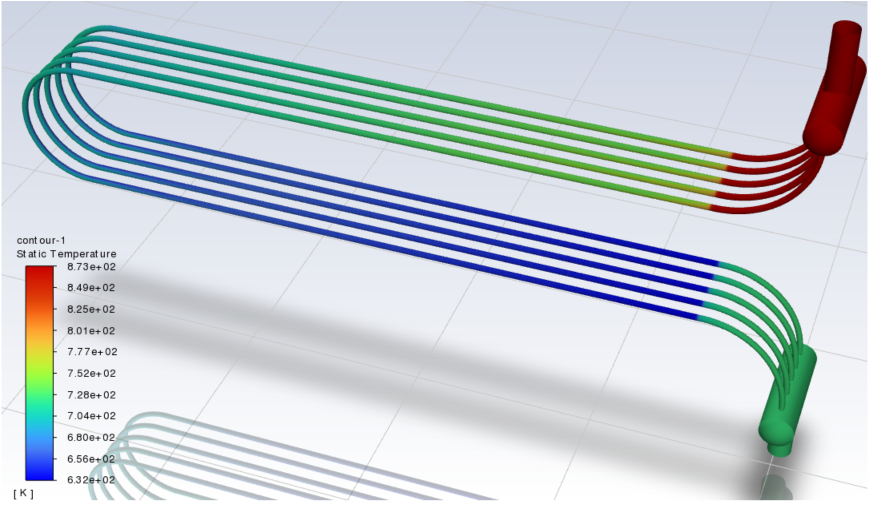

Figure 5.14: Temperature Contours of inner walls for Case 2 - 1 [bar]

FEM simulation with Remote Displacement Support

Contours of Von Mises stress of Case 2 with remote displacement support can be seen in Fig.5.15. The lower manifold was suppressed in the FEM simulation in order to decrease the number of elements and simplify the simulation in order to save time. As can be seen, the stress in the manifolds is close to 0 as the temperature is almost uniform. This proves that the investigation of the lower manifold is negligible. Thus, the lower manifold will be suppressed for every upcoming FEM analysis. Moreover, the U-shaped part is identified as the maximal stress location and the mesh is refined for better visualisation of the area.The distribution of the thermal stress clearly shows an effect of secondary flow circulation across the whole domain, especially at the U-shaped part of the pipes, where the maximum stress occurs. The maximum stress has reached a magnitude of 64.1 [MPa].

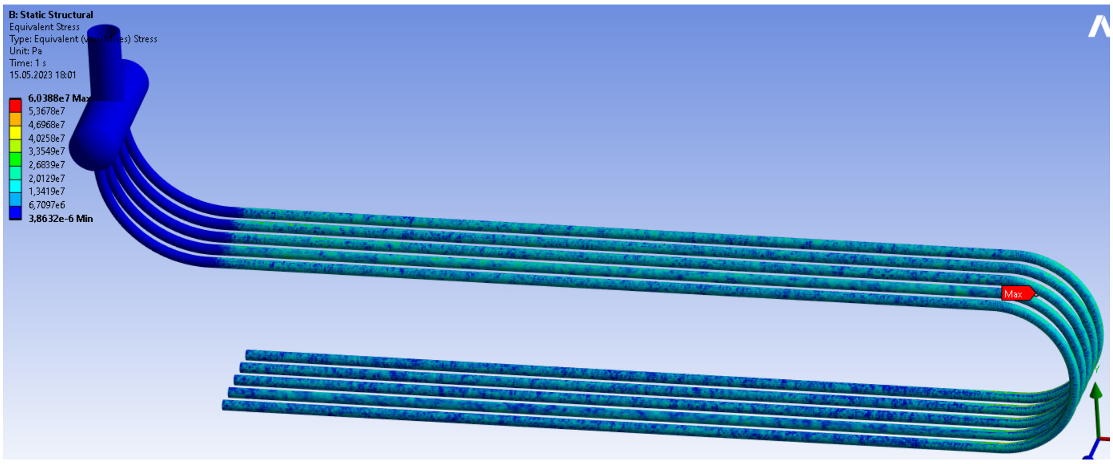

Figure 5.15: Contours of Von Mises stress for Case 2 - 1 [bar] with Remote displacement support

The Fig.5.16, shows a comparison between the temperature map and contours of Von Mises stress for the investigated case at the location of the maximal stress. The maximal stress is located at the upper part of the U-shaped part of the pipe. This is probably caused similarly as in the previous case by the secondary flow circulation. As the bent parts of the pipe seem to be the main location of thermal stress, the maximal stress location is expected to appear at the bent shape where the temperature of the fluid is highest and the external convection is happening, which is, in this case, the U-shape part.

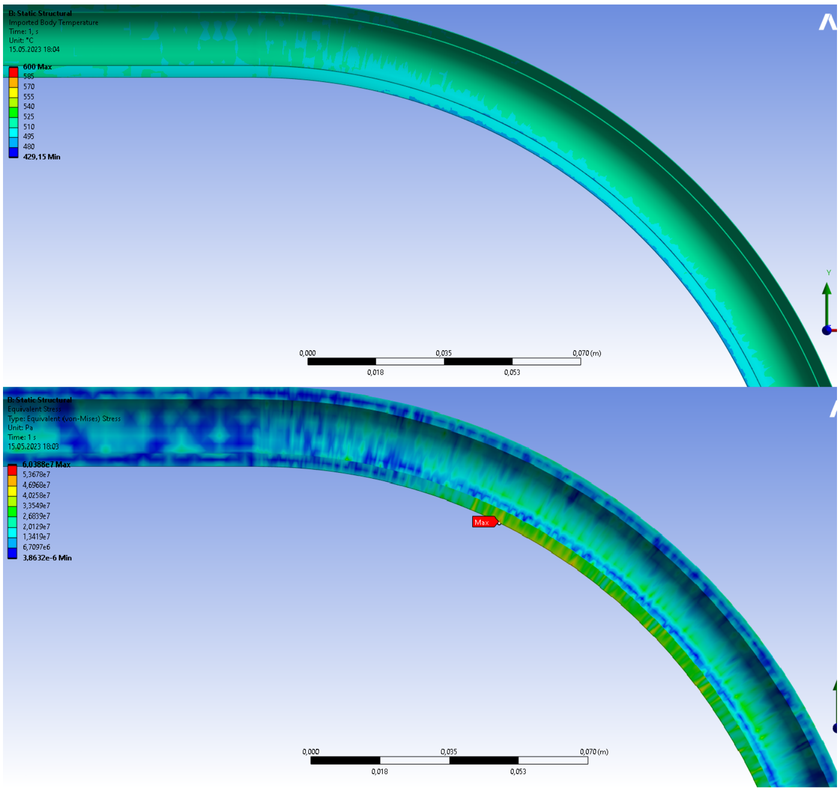

Figure 5.16: Contours of Temperature (upper) and Von Mises stress (lower) of the upper part of the U-shape for Case 2 - 1 [bar] with Remote displacement support

FEM simulation with Fixed Support

As has been stated in the previous chapter, so far presented simulations of the thermal stress are assuming, that the expansion of the pipes into the baffle is protected by sealing or other elastic parts, which are absorbing the stress due to constrained expansion. In this scenario, the assumption that the baffle is connected directly to the pipes is applied in the form of Fixed support which constrains expansion in all directions. The contour of Von Mises stress then can be seen in Fig.5.17. In this case, the dominant mechanism of stress is the constrained expansion of the pipes at the location of the baffle. Even though there can be seen locations of increased stress along the lower radius of the U-shape bent. The magnitude of the thermal stress at the baffle is higher by almost whole order.

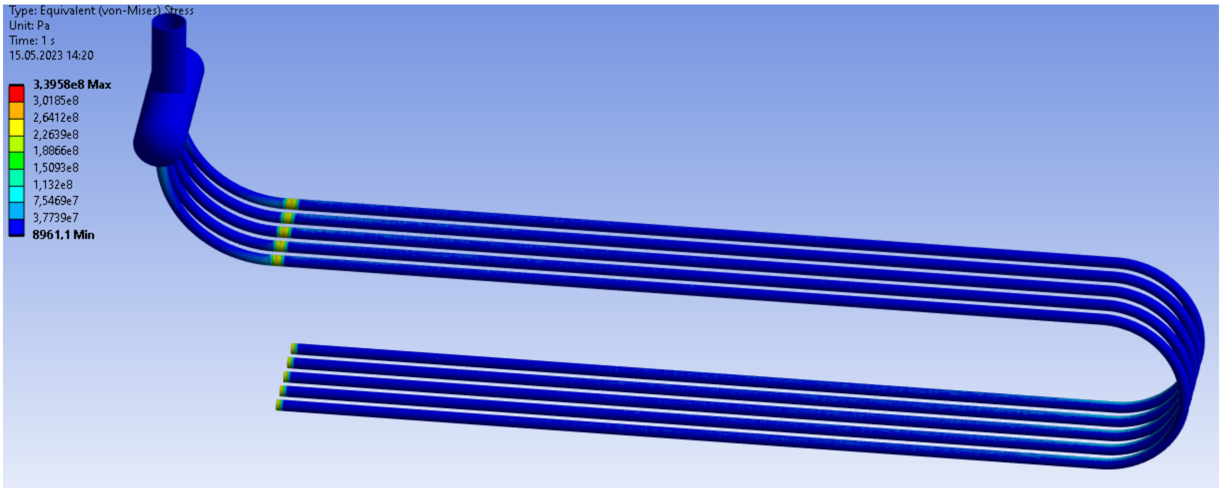

Figure 5.17: Contours of Von Mises stress for Case 2 - 1 [bar] with Fixed Support

The maximum stress location and stress distribution can be seen in Fig.5.18. The baffle location is represented by the outer diameter of the pipe on the border adiabatic and convection boundary conditions used in the CFD simulation. In a real application, the line with the highest stress magnitude would be wider as the baffle would be thicker than the circle that represents the connection. The contours of Von Mises stress are showing an effect of stress caused by constrained expansion, which is symmetrically distributed at both sides of the pipe. The maximal stress for Case 2 with Fixed support and atmospheric pressure is 340 [MPa].

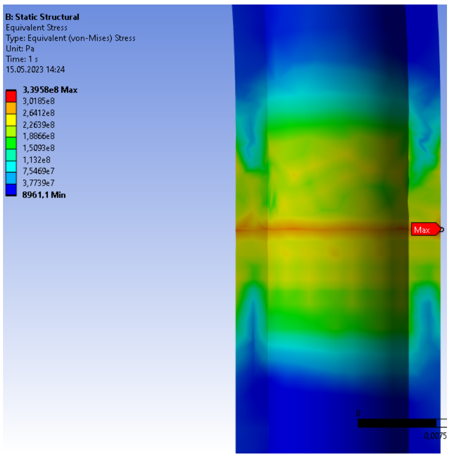

Figure 5.18: Detail on Maximum stress location of Case 2 - 1 [bar] with Fixed Support

5.2.2 Scenario with the pressure of working fluid 2 bar

Temperature contours of a cross-section of the investigated scenario can be seen in Fig.5.19. The distribution of temperature is similar to the previous scenario but with a higher minimum temperature. Thermal stress can be expected due to the temperature difference across the thickness of the pipe.

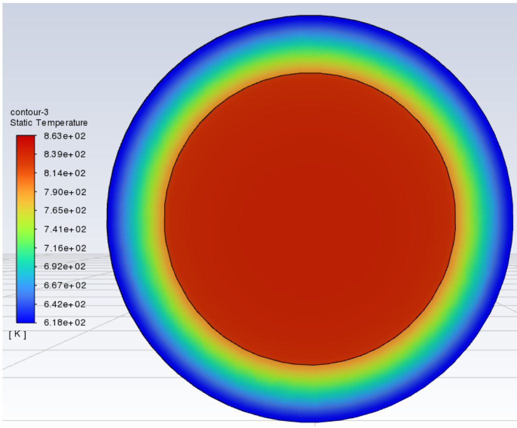

Figure 5.19: Temperature Contours of a cross-section of pipe for Case 2 - 2 [bar]

Temperature contours of the inner walls of the heat exchanger can be seen in Fig.5.20. A stable decrease in temperature across the length of the pipes is shown. Similarly, as in the previous case, there is a border between the convection region and the adiabatic region, which can be easily observed.

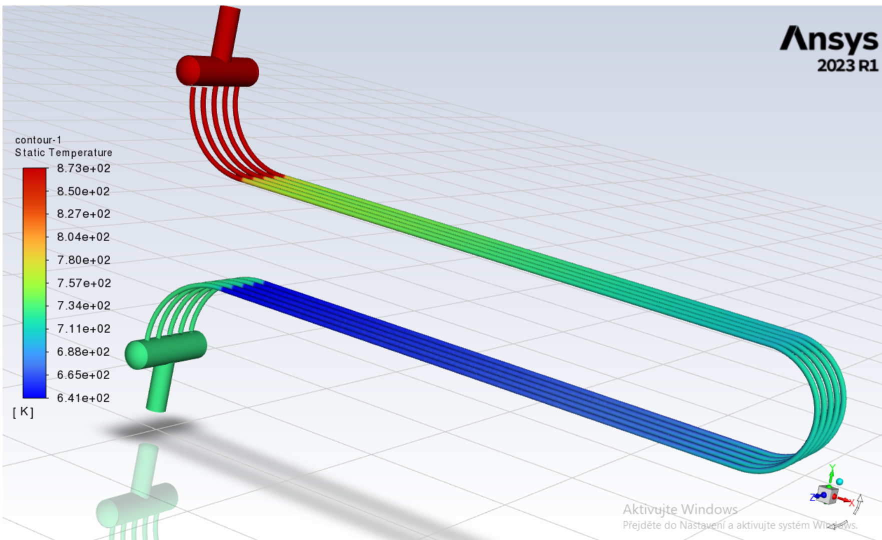

Figure 5.20: Temperature Contours of inner walls for Case 2 - 2 [bar]

The contours of Von Mises stress can be seen in Fig.5.21. The whole length of the tube is covered by thermal stress in the magnitude between 1- 20 [MPa]. The maximal stress is located at the upper part of the U-shape as in the previous case and has a magnitude of 54.5 [MPa].

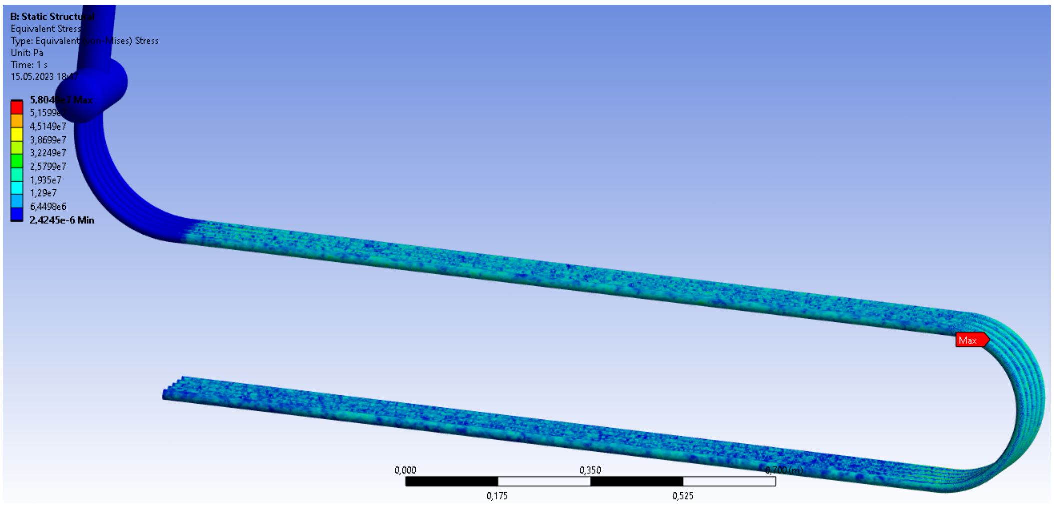

Figure 5.21: Contours of Von Mises stress for Case 2 - 2 [bar]

A detailed look at the location of maximal stress together with a comparison of the temperature map can be seen in Fig.5.22. Large temperature differences can be seen at the smaller radius of the U-shape, which causes higher magnitudes of thermal stress.

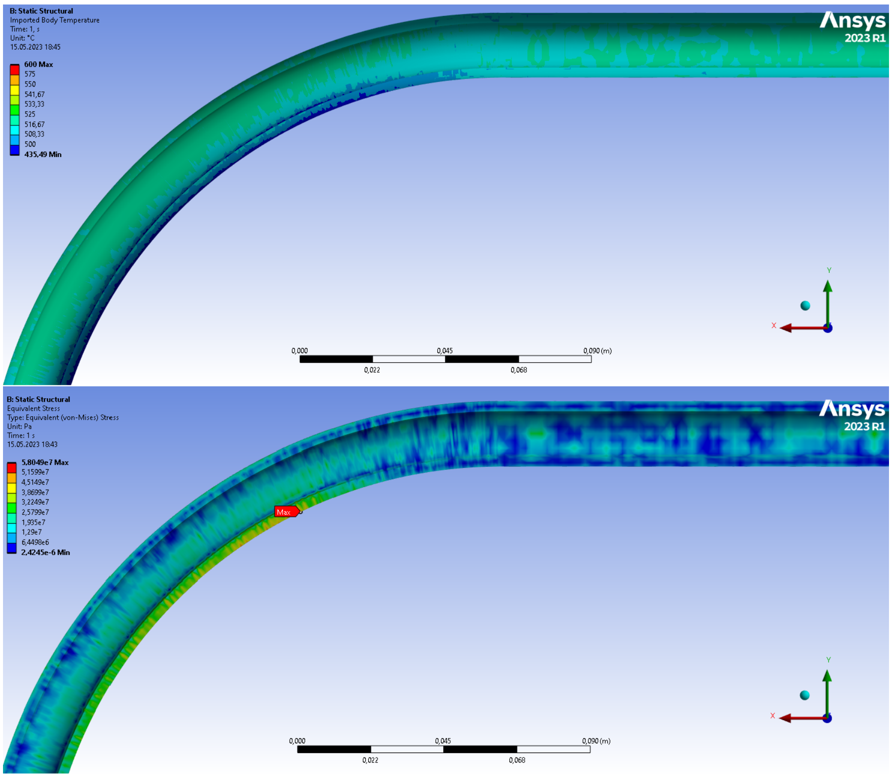

Figure 5.22: Contours of Temperature (upper) and Von Mises stress (lower) of the upper part of the U-shape for Case 2 - 2 [bar]

5.2.3 Scenario with the pressure of working fluid 5 bar

The scenario of Case 2 with boiling water pressurized to 5 [bar] is investigated in this section. Temperature contours of a cross-section of pipe can be seen in Fig.5.23.

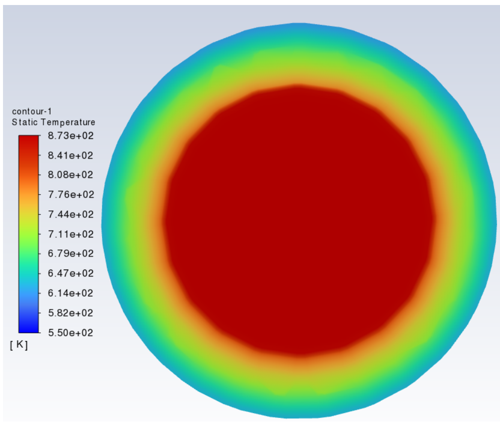

Figure 5.23: Temperature Contours of a cross-section of pipe for Case 2 - 5 [bar]

The temperature contours of the inner walls of investigated scenario can be seen in Fig.5.24. In a closer look at the U-shape part, one can see thermal gradients occurring at the location.

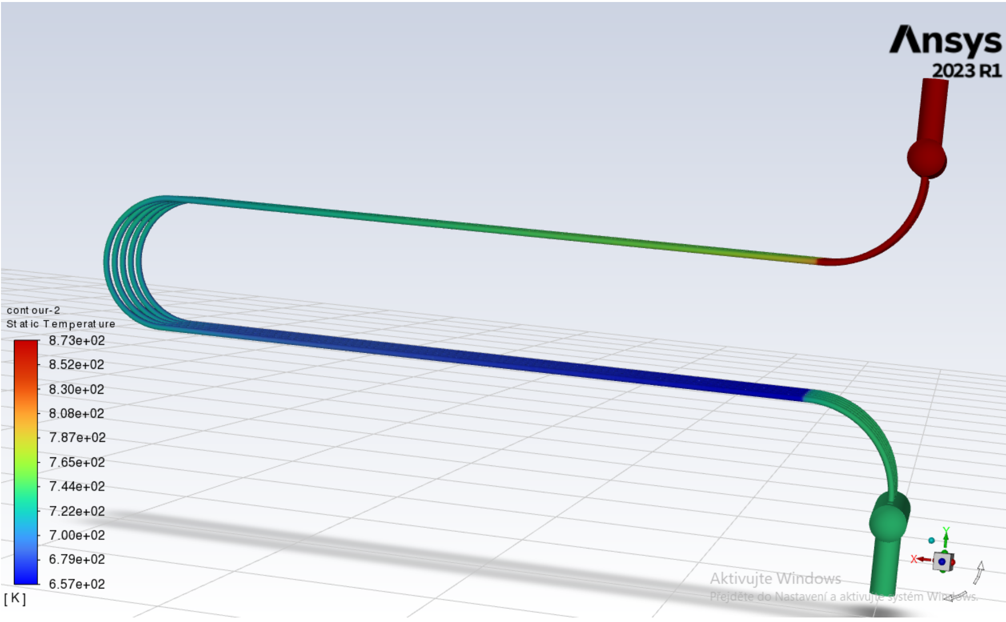

Figure 5.24: Temperature Contours of inner walls for Case 2 - 5 [bar]

Similarly, to the previous simulation, FEM analysis is performed. The results in the form of Von Mises stress are displayed in Fig.5.25. The stress distribution is as expected similar to the previous cases, as the only difference between the simulations is the temperature of the surrounding water.

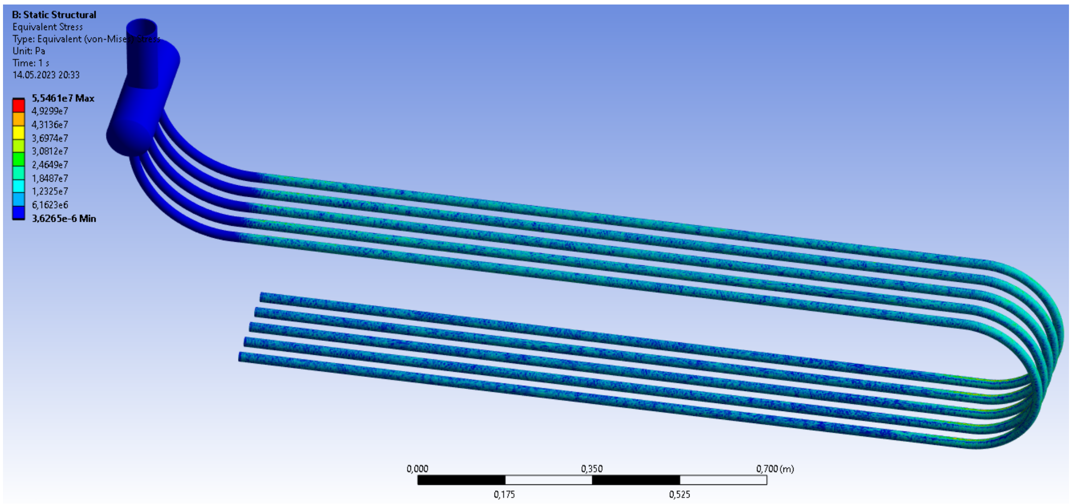

Figure 5.25: Contours of Von Mises stress for Case 2 - 5 [bar]

A graphical comparison between the temperature map and Von Mises stress contours at the upper part of the U-shape can be seen in Fig.5.26. The stress contours are similar to the previous cases and display increased stress concentration at the smaller radius of the bent. The maximal stress in the investigated case has a magnitude of 55.5 [MPa]

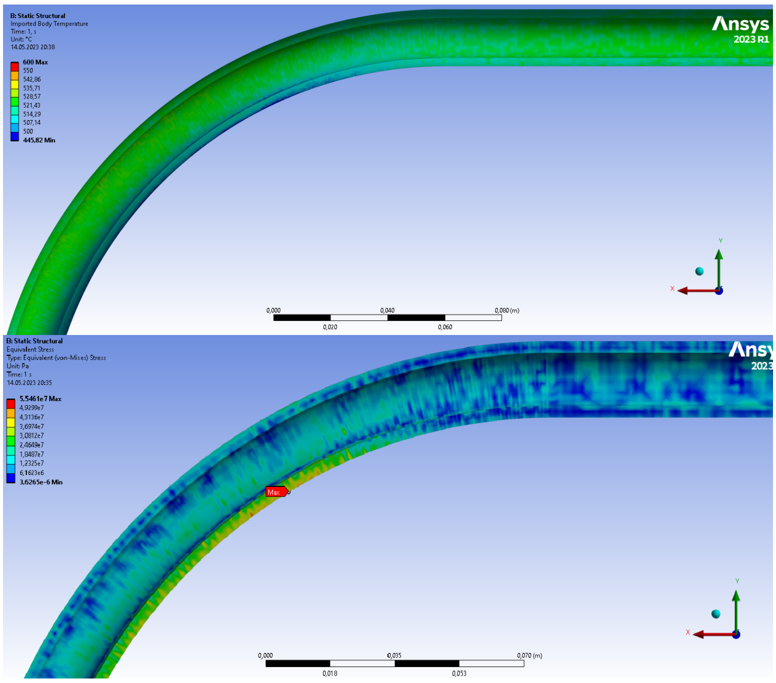

Figure 5.26: Contours of Temperature (upper) and Von Mises stress (lower) of the upper part of the U-shape for Case 2 - 5 [bar]

5.3 Comparison of Factor of Safety

The Factor of Safety (FOS) or Coefficient of Safety is the rate between tensile yield strength or tensile ultimate strength of the material and the maximum stress at the model. Determining the appropriate safety factor is a complex and responsible task. A high safety factor usually leads to a safer design at the cost of higher weight and thus higher prices, and vice versa. This is a basic engineering compromise of "price versus safety". Professional organisations often specify minimum safety coefficients for various systems, but it is entirely the designer's responsibility to determine such a safety coefficient that would guarantee adequate safety while maintaining an acceptable price. At the same time, the safety coefficient can vary in a very wide range. The basic definition for considering tensile yield strength is as follows:

- The value of Factor of Safety is less than 1. Therefore the stress in the material exceeded the elastic range
- The value of Factor of Safety is 1. Therefore the stress in the material is equal to the tensile yield strength
- The value of Factor of Safety is more than 1. Therefore the stress in the material is in the elastic range

The tensile yield strength for Inconel 600 is equal to TYS = 240.6 [MPa] according to the Ansys Mechanical database. The factor of safety is then calculated as follows:

$$FOS = \frac{TYS}{\sigma_{max}} \tag{5.1}$$

where σ_{max} is the maximal stress in the model.

The resulting maximal stress and Factor of Safety for every simulation can be seen on Tab.5.1. As expected, the scenario with water pressure at the atmospheric level produces the highest value of thermal stress (Case 1 - $\sigma_{max} = 27.5[MPa]$ & FOS = 8.75 [-], Case 2 - $\sigma_{max} = 60.4[MPa]$ & FOS = 3.98 [-]) and thus the smallest value of the Factor of Safety for both investigated cases. Moreover, it has been revealed that in a situation, where the baffle would be pressed on the pipes, the stress caused by constrained expansion would exceed the tensile yield stress as the value for Factor of Safety is less than 1. This would result in exceeding the elastic range and irreversible strain, which could result in necking or fracture if the stress would increase. In this scenario, it would be necessary to either apply elastic parts between the baffle and the pipes, which would absorb the stress caused by the expansion or change the material to one with higher tensile yield strength.

Scenario	Water pressure [bar]	Maximum stress [MPa]	Safety Factor [-]
Case 1	1	27.5	8.75
	2	22.8	10.56
	5	24.8	9.72
Case 2	1	60.4	3.98
	2	54.5	4.42
	5	55.5	4.34
Case 2 -Fixed Support	1	340	0.71

Table 5.1: Results of investigated cases, Maximum stress and Factor of Safety

Fig.5.27 shows a graphical display of the maximal stress and Factor of Safety magnitude in relation to the pressure of the surrounding boiling water. As previously stated, the highest values of maximal stress and the lowest value of the Factor of Safety for both cases occur at pressure 1 [bar]. It was expected that the lowest magnitude of stress and thus the maximal value of FOS will appear at the highest pressure as the temperature of the surrounding water is higher than for the rest of the scenarios, which should produce lower thermal gradients and thus lower magnitudes of thermal stress, but it seems like the minimal thermal stress and the maximum FOS happens at water pressure 2 [bar]. Another thing that should be mentioned is that the values of stress for Case 1 are significantly higher than for Case 2. This is probably caused by multiple factors, one of them is that because there are multiple pipes in Case 2, the mass flow rate is divided between each of them, which results in lower velocity and less influence of the secondary flow circulation the bent of the pipes. Also, the heat transfer fluid (molten NaOH) temperature decreases more before reaching the first bent, which results in lower temperature gradients in the bent. The temperature of the NaOH in the bent is also lower due to the higher area of heat transfer, which results in higher heat flux. In summary, since the values of Factor of Safety are more than one for all investigated cases with Remote Displacement Support all the different Water pressures can be used as long as the expansion between tubes and baffle is covered by an elastic part.

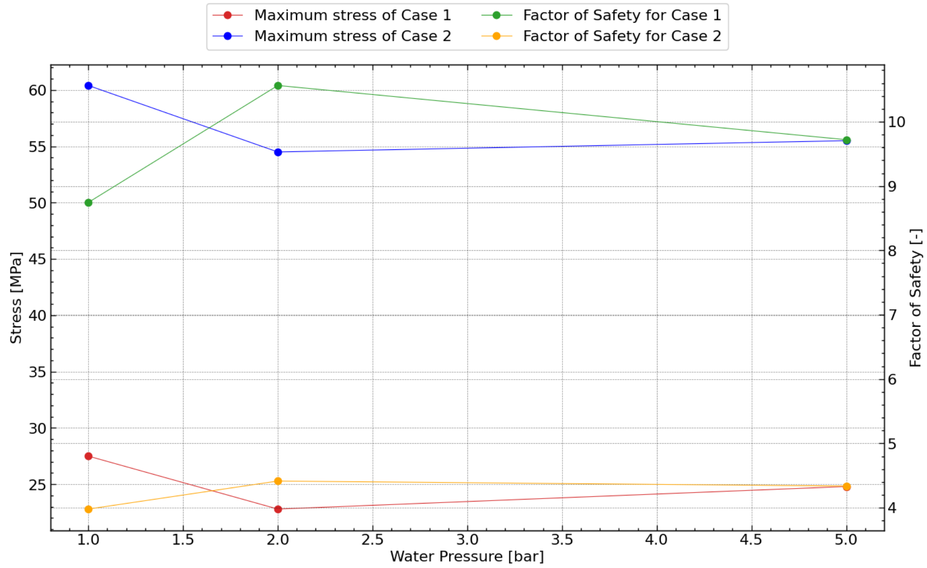

Figure 5.27: Graphic comparison between results of investigated cases with Remote Displacement Support, Effect of water pressure on maximum stress and factor of safety

Chapter 6

Conclusion

In conclusion, the integration of energy storage technologies is crucial for achieving a flexible power grid that effectively incorporates renewable energy sources. Among the various energy storage methods, Molten Salt Energy Storage Systems (MOSESS) have shown great potential due to their unique thermo-physical characteristics. However, the design of molten salt heat exchangers poses challenges, particularly in managing thermal stresses resulting from temperature differentials between hot and cold fluids.

Through the use of computational fluid dynamics (CFD) coupled with Finite Element Method (FEM) analysis, engineers can gain valuable insights into the magnitude of thermal stress and make informed decisions to enhance the design quality of molten salt heat exchangers. This analysis helps determine the suitability of materials and the need for modifications to the heat exchanger's geometry. Thus the thermal stress analysis is performed for 2 types of design of heat exchangers, namely double pipe HX and U-tube HX. The materials used in the analysis are Nickel alloy Inconel 600 for the solid parts and molten Sodium Hydroxide for the heat transfer fluid. The heat transfer is assumed to be fully represented by the external convection of boiling water at the outer sides of the pipes.

The results of the simulations revealed that the scenario with water pressure at the atmospheric level produced the highest thermal stress (Case 1 - $\sigma_{max} = 27.5[MPa]$ & Case 2 - $\sigma_{max} = 60.4[MPa]$), while the scenario with water pressure at 2 bar resulted in the lowest stress (Case 1 - $\sigma_{max} = 22.8[MPa]$ & Case 2 - $\sigma_{max} = 54.5[MPa]$)and the highest Factor of Safety (Case 1 - FOS = 10.56 [-] & Case 2 - FOS = 4.42 [-]). Additionally, it was found that when the baffle was pressed on the pipes, the stress caused by constrained expansion exceeded the tensile yield strength for Inconel 600 (TYS = 240.6 [MPa]), since the values for maximal thermal stress is $\sigma_{max} = 340[MPa]$, which is higher than the tensile yield strength, and Factor of safety (FOS = 0.71 [-]), which is less than 1 and therefore the connection is necessitating the use of elastic parts or materials with higher tensile yield strength. Consequently, it can be concluded that as long as the expansion of the pipes is unconstrained (by application of elastic materials like sealing between the baffle and the pipes) the thermal stress should not cause any permanent damage as the magnitude of the stress does not exceed the elastic range.

Although, it would be beneficial for future investigation to perform Mesh Independency analysis for Case 2 to avoid any numerical errors or to avoid not capturing some fluid phenomenon due to the coarseness of the mesh. Moreover, the mesh for the FEM analysis produces contours, which are not fully in agreement with the expectation, but a finer mesh would be too computationally demanding and the simulation would not finish. Therefore, the simulation could be done again with much finer mesh in a computer with higher installed RAM.

Overall, the findings emphasize the importance of proper design and careful operation to ensure the safe and efficient performance of molten sodium hydroxide heat exchangers. The use of CFD and FSI analysis enables engineers to optimize the design, ensuring that the thermal stresses remain within the acceptable range and that the chosen materials are suitable for the operating conditions. Moreover, it should be mentioned that despite the expectation, the highest investigated pressure of surrounding water did not result in the lowest stress magnitudes. Although, the simulation results could be affected by uncertainties in the model and numerical modelling. Moreover, more water pressures should be investigated to confirm or disprove this study's outcomes.

By implementing these design strategies and utilizing computational analysis techniques, the performance and safety of molten sodium hydroxide heat exchangers can be improved. This, in turn, contributes to the successful integration of MOSESS into the power grid, supporting the goal of achieving a more flexible and sustainable energy system.

It should be noted that further research and experimentation may be necessary to validate and refine the findings presented in this study. Nonetheless, the insights gained from this research provide a foundation for future advancements in the field of energy storage and contribute to the overall understanding of thermal stress management in molten sodium hydroxide heat exchangers.

In conclusion, the combination of innovative design approaches, careful operation, and the utilization of computational analysis tools holds great promise for optimizing the performance, safety, and efficiency of molten sodium hydroxide heat exchangers, paving the way for the widespread implementation of MOSESS in the transition towards a more sustainable energy future.

Chapter 7

Further Work

A numerical investigation of molten sodium hydroxide heat exchanger in this study involves a complex process in which several parameters must be accounted for. Thus, there are still other aspects that need to be taken into consideration which could be done throughout the research, but due to the time limit, some of the other possible procedures will be explained as further work.

For instance, instead of running steady-state simulations, which do not take into account stress cycling. The simulation could be changed to transient. This could take into consideration the start-up procedure, where the initial temperature of the pipes is much smaller than the molten sodium hydroxide. This would produce much higher thermal stress than the investigated scenarios since the thermal gradients would be higher.

Another change in the simulation setup could be done by simulating the whole heat exchanger with a working fluid flow. The simulation would then have to be multiphase as the water is expected to boil. This would exchange the constant values of Freestream temperature and Convection heat transfer coefficient for a more accurate description of the process.

Furthermore, the FEM analysis could be improved by modelling the baffle, which would provide a more accurate description of the scenario, where the baffle is pressed on the pipes. This would generate more accurate results regarding the stress induced by constrained expansion. Next, the sealing between the baffle and the pipes could be included. This simulation could be beneficial to indicate what size and materials can be used to mitigate the risk of damaging the heat exchanger's pipes.

Bibliography

[1] Michael Green et al. “Nuclear Hybrid Energy System: Molten Salt Energy Storage”. In: ().

[2] Nesrine Jaziri et al. “A Comprehensive Review of Thermoelectric Generators: Technologies and Common Applications”. In: *Energy Reports*. SI:Energy Storage - Driving towards a Clean Energy Future 6 (Dec. 1, 2020), pp. 264–287. DOI: 10.1016/j.egyr.2019.12.011.

[3] *HA Technology Now Available at Industry-First 64 Percent Efficiency | GE News*. URL: https://www.ge.com/news/press-releases/ha-technology-now-available-industry-first-64-percent-efficiency (visited on 02/24/2023).

[4] Xing Luo et al. “Overview of Current Development in Electrical Energy Storage Technologies and the Application Potential in Power System Operation”. In: *Applied Energy* 137 (Jan. 1, 2015), pp. 511–536. DOI: 10.1016/j.apenergy.2014.09.081.

[5] Muhammad Tawalbeh et al. “A comprehensive review on the recent advances in materials for thermal energy storage applications”. In: *International Journal of Thermofluids* 18 (2023), p. 100326. DOI: https://doi.org/10.1016/j.ijft.2023.100326.

[6] B. D’Aguanno et al. “Thermostatic Properties of Nitrate Molten Salts and Their Solar and Eutectic Mixtures”. In: *Scientific Reports* 8.1 (July 11, 2018), p. 10485. DOI: 10.1038/s41598-018-28641-1.

[7] S. M. Hasnain. “Review on Sustainable Thermal Energy Storage Technologies, Part I: Heat Storage Materials and Techniques”. In: *Energy Conversion and Management* 39.11 (Aug. 1, 1998), pp. 1127–1138. DOI: 10.1016/S0196-8904(98)00025-9.

[8] Zhen Yang and Suresh V. Garimella. “Cyclic Operation of Molten-Salt Thermal Energy Storage in Thermoclines for Solar Power Plants”. In: *Applied Energy* 103 (Mar. 1, 2013), pp. 256–265. DOI: 10.1016/j.apenergy.2012.09.043.

[9] H. Kobayashi et al. “Thermal Conductivity, Viscosity, and Electrical Conductivity of Molten NaOH”. In: *The Journal of Chemical Physics* 2001 (115(23), pp. 10931–10938. DOI: 10.1063/1.1416135.

[10] Che Nor Aniza Che Zainul Bahri et al. “Characteristic of Molten Fluoride Salt System LiF-BeF2 (Flibe) and LiF-NaF-KF (Flinak) as Coolant and Fuel Carrier in Molten Salt Reactor (MSR)”. In: MATHEMATICAL SCIENCES AND ITS APPLICATIONS. Uttar Pradesh, India, 2017, p. 040008. DOI: 10.1063/1.4972932.

[11] G. P. Dukhanin and S. I. Lopatin. "Thermodynamic Properties of NaNO3-KNO3 Melts". In: *Russian Journal of General Chemistry* 89.3 (Mar. 1, 2019), pp. 470–474. DOI: 10.1134/S1070363219030174.

[12] James Pacheco, Steve Showalter, and William Kolb. "Development of a Molten-Salt Thermocline Thermal Storage System for Parabolic Trough Plants". In: *Journal of Solar Energy Engineering* 124 (May 1, 2002), p. 153. DOI: 10.1115/1.1464123.

[13] Kalawole Muritala I. Makinta B. Tizane D. Guy Christian T. Jacques N. Téré D. Antoine B. and Rabani A. Boubou B. "Review on Thermocline Storage Effectiveness for Concentrating Solar Power Plant". In: *Energy and Power Engineering* 2021.13 (), pp. 343–364. DOI: 10.4236/epe.2021.1310024..

[14] Piyush Sabharwall et al. "Advanced Heat Exchanger Development for Molten Salts". In: *Nuclear Engineering and Design* 280 (Dec. 1, 2014), pp. 42–56. DOI: 10.1016/j.nucengdes.2014.09.026.

[15] Zhihao Xu et al. "High-Temperature Corrosion Behavior of Inconel 625 Alloy in a Ternary Molten Salt of NaCl-CaCl2-MgCl2 in Air and N2". In: *Solar Energy* 238 (May 15, 2022), pp. 216–225. DOI: 10.1016/j.solener.2022.03.074.

[16] M. Pooja, K.S. Ravishankar, and Vasudeva Madav. "High temperature corrosion behaviour of stainless steels and Inconel 625 in hydroxide salt". In: *Materials Today: Proceedings* 46 (Mar. 2021). DOI: 10.1016/j.matpr.2021.02.266.

[17] Ya-Ling He et al. "Experimental Investigation on Turbulent Heat Transfer Characteristics of Molten Salt in a Shell-and-Tube Heat Exchanger". In: *Applied Thermal Engineering* 108 (Sept. 5, 2016), pp. 1206–1213. DOI: 10.1016/j.applthermaleng.2016.08.023.

[18] Arvengtraining. *Basics of Shell & Tube Heat Exchangers*. Arveng Training & Engineering. URL: https://arvengtraining.com/en/basics-of-shell-tube-heat-exchangers/ (visited on 03/27/2023).

[19] H. Sohn et al. "20 - Sensing Solutions for Assessing and Monitoring of Nuclear Power Plants (NPPs)". In: *Sensor Technologies for Civil Infrastructures*. Ed. by M. L. Wang, J. P. Lynch, and H. Sohn. Vol. 56. Woodhead Publishing Series in Electronic and Optical Materials. Woodhead Publishing, Jan. 1, 2014, pp. 605–637. ISBN: 978-1-78242-242-6. DOI: 10.1533/9781782422433.2.605.

[20] Mourad Dougdag, Rafaël Fernandez, and Damien Lamberts. "Risk Reassessment of Thermal Striping Due to a Macro-Crack Pre-Existent in Nuclear Reactors at High Temperature". In: *Annals of Nuclear Energy* 174 (Sept. 1, 2022), p. 109152. DOI: 10.1016/j.anucene.2022.109152.

[21] Yan Luo et al. "Analysis of Thermal Stress, Fatigue Life and Allowable Flux Density for the Molten Salt Receiver in Solar Power Tower Plants". In: *International Journal of Low-Carbon Technologies* 17 (Feb. 8, 2022), pp. 1385–1398. DOI: 10.1093/ijlct/ctac110.

[22] *IBM Documentation*. Apr. 14, 2021. URL: https://www.ibm.com/docs/en/power9/0009-ESS?topic=exchangers-water-specifications-secondary-cooling-loop (visited on 05/08/2023).

[23] Andrew R. Gow and Salim M. Salim. "Analysis of Thermal Mixing in T-junctions Using Fluid-Structure Interaction: 2018 International MultiConference of Engineers and Computer Scientists, IMECS 2018". In: *Proceedings of the International MultiConference of Engineers and Computer Scientists 2018, IMECS 2018*. Lecture Notes in Engineering and Computer Science (Mar. 14, 2018). Ed. by Oscar Castillo et al. URL: http://www.scopus.com/inward/record.url?scp=85062591140&partnerID=8YFLogxK (visited on 04/28/2023).

[24] V. S. Naik-Nimbalkar et al. "Thermal Mixing in T-junctions". In: *Chemical Engineering Science* 65.22 (Nov. 15, 2010), pp. 5901–5911. DOI: 10.1016/j.ces.2010.08.017.